Microstructure Estimates of Turbulent Salinity Flux and the Dissipation Spectrum of Salinity

JONATHAN D. NASH* AND JAMES N. MOUM

College of Oceanic and Atmospheric Sciences, Oregon State University, Corvallis, Oregon

(Manuscript received 26 September 2000, in final form 3 January 2002)

ABSTRACT

Direct determination of the irreversible turbulent flux of salinity in the ocean has not been possible because of the complexity of measuring salinity on the smallest scales over which it mixes. Presented is an analysis of turbulent salinity microstructure from measurements using a combined fast-conductivity/temperature probe on a slowly falling vertical microstructure profiler. Four hundred patches of ocean turbulence were selected for the analysis. Highly resolved spectra of salinity gradient Ψ_{S_z} exhibit an approximate k^{+1} dependence in the viscous–convective subrange, followed by a roll-off in the viscous–diffusive subrange, as suggested by Batchelor, and permit the dissipation rate of salinity variance χ_S to be determined. Estimates of irreversible salinity flux from measurements of the dissipation scales (from χ_S, following Osborn and Cox) are compared to those from the correlation method ($\langle w'S' \rangle$), from TKE dissipation measurements (following Osborn), and to the turbulent heat flux. It is found that the ratio of haline to thermal turbulent diffusivities, $d_\chi = K_S/K_T = \chi_S/\chi_T(dT/dS)^2$ is $0.6 < d_\chi < 1.1$.

1. Introduction

Despite the two order of magnitude discrepancy between the molecular diffusivities of heat ($D_T \simeq 10^{-7}$ m^2 s^{-1}) and salt ($D_S \simeq 10^{-9}$ m^2 s^{-1}), it is commonly assumed that turbulent transports of heat and salt are equal. It is presumed that turbulent fluxes are dominated by the motions of the largest-scale eddies and that molecular processes (which produce the irreversible mixing) occur at a rate consistent with the large-scale turbulence production. In calculating salt fluxes, this has been a necessary assumption because it has not been possible to directly measure the turbulent flux of salt or the dissipation rate of salinity variance.

It is well known that double-diffusive processes transport heat and salt at different rates (Schmitt 1979). The unique dynamics associated with these structures are a direct consequence of the large value of the ratio $D_T/D_S \simeq 100$, but only occur when turbulence is weak and for a limited range of dT/dS. Having potentially broader implications are the poorly understood processes in turbulent mixing events that may lead to a differential transport of heat and salt (Gargett 2002). Both laboratory (Turner 1968; Altman and Gargett 1990) and numerical experiments (Merryfield et al. 1998; Holloway et al. 2001) indicate that heat is transported more effectively than salt in weak, stratified turbulence. This discrepancy in mixing efficiencies has been attributed to the incomplete mixing of salt. Since all previous research represents mixing in weak, low Reynolds number turbulence, it remains an open question as to whether the turbulent transports of heat and salt are significantly different in high Reynolds number ocean turbulence (Gargett 2002). Only scaling arguments have been available to estimate the role salinity plays in the eddy diffusivity for mass (or buoyancy) and its importance in the generation of entropy (Gregg 1984).

While estimates of K_T (the eddy diffusivity for heat) using the methods of Osborn and Cox (1972) have been made over the past 30 years, K_S (the eddy diffusivity for salt) has eluded measurement. In particular, it has not been possible to measure the spectrum of salinity gradient Ψ_{S_z} nor determine its integral, the dissipation rate of salinity variance χ_s, for two reasons. First, the spectrum of salinity gradient peaks at scales $10\times$ smaller than that of temperature gradient. Salinity must be measured at submillimeter scales to resolve the salinity gradient at typical turbulent kinetic energy dissipation rates. Second, salinity (S) cannot be measured directly. Instead, independent, collocated measurements of conductivity (C) and temperature (T) must be combined to determine S. As a result, the spectrum of salinity gradient must be formed as the composite spectrum of tem-

* Current affiliation: Applied Physics Laboratory, University of Washington, Seattle, Washington.

Corresponding author address: Jonathan Nash, College of Oceanic and Atmospheric Sciences, Oregon State University, 104 Ocean Admin. Bldg., Corvallis, OR 97331-5503.
E-mail: nash@coas.oregonstate.edu

perature gradient, conductivity gradient, and their cospectrum—each of which must be adequately resolved.

The basic assumption that all scalars are transported equally by turbulence, regardless of their molecular diffusivities, stems from the reasoning that turbulent transports generally occur at scales much larger than the scales of molecular processes. This separation of scales is often a fundamental premise of high Reynolds number turbulence theory and analysis. Assuming the typical cascade of energy, turbulent fluctuations are produced at the scales of the largest eddies and break down into smaller and smaller eddies where they are eventually dissipated by molecular diffusion.

Assuming homogeneous turbulence, the equation governing the evolution of fluctuating scalar variance $\langle \theta'^2 \rangle$ is (Osborn and Cox 1972)

$$\frac{D}{Dt}\langle \theta'^2 \rangle - P_\theta = -\chi_\theta, \tag{1}$$

where $P_\theta = -2\langle u_i' \theta' \rangle \langle d\theta/dx_i \rangle$ represents the gradient production of $\langle \theta'^2 \rangle$ and $\chi_\theta = 2D_\theta \langle (\nabla\theta)^2 \rangle$. Since most of the variance of u_i' and θ' occurs at scales associated with the largest eddies, the effect of molecular diffusivity on P_θ should be small. It is hence believed that the turbulent transport of all scalars should be equal because it is governed by the evolution of the large-scale velocity field acting on mean gradients, (P_θ, the production) and not by molecular diffusion (χ_θ, the dissipation). A fundamental assumption is that molecular diffusion occurs at a rate governed by the largest-scale motions in order to fulfill the $P_\theta = \chi_\theta$ balance. For the case of steady-state, homogeneous, high-Re turbulence, this condition should indeed be satisfied. In the ocean, however, it is likely that this balance is seldom achieved due to the inherent space–time variability of geophysical turbulence. Numerical simulations of a Kelvin–Helmholtz billow (Smyth 1999) illustrate one such evolution. Our inadequate sampling further precludes the full accounting of terms in Eq. (1).

The assumption of $P_\theta = \chi_\theta$ provides one means of estimating χ_S from χ_T and the mean gradients of T and S. Since P_θ results entirely from turbulent overturns acting on mean gradients, then $P_T/P_S = (dT/dS)^2$. This has led to the convenient scaling of χ_S in the past (Gregg 1984, 1987; Gargett and Moum 1995):

$$\chi_S = \left(\frac{dS}{dT}\right)^2 \chi_T. \tag{2}$$

Following Osborn and Cox (1972), we define the eddy diffusivity by considering Eq. (1) for the case of isotropic turbulence where the background state has only a mean vertical gradient. The vertical eddy flux $\langle w'\theta' \rangle$ may be expressed in terms of the turbulent diffusivity K_θ, such that $\langle w'\theta' \rangle = K_\theta \langle \partial\theta/\partial z \rangle$. Substituting this into Eq. (1), the eddy diffusivity is

$$K_\theta = \frac{\chi_\theta/2}{\langle (\partial\theta/\partial z) \rangle^2}. \tag{3}$$

As a result of Eqs. (2) and (3), the eddy diffusivities of heat K_T and salt K_S have been assumed equal. However, recent numerical investigations by Merryfield et al. (1998) suggest that these may indeed be different, especially at low turbulence intensities.

Of fundamental importance to the turbulent transport of salinity is the determination of the spectral shape of salinity gradient fluctuations and the dissipation rate of salinity variance. Quantification of Ψ_{S_z} and χ_S is the primary goal of this analysis. Measurements of highly resolved salinity also permit direct estimation of salinity flux $\langle w'S' \rangle$ (Moum 1990).

This paper is organized as follows. In section 2, the general form of the spectrum of salinity gradient is developed, and the experimental and analytical procedures used to obtain it are described. Observations of gradient spectra, scalar dissipation rates, and covariance fluxes are presented in section 3. In the discussion (section 4), normalized spectra are presented, and the turbulent fluxes of salinity and temperature are compared in terms of dissipation flux coefficients Γ_o and Γ_d and diffusivity ratios d_o and d_χ. We discuss how our flux estimates and the observed spectral shapes may be consistent with differential diffusion. We conclude (section 5) that the spectrum of salinity gradient has a shape similar to that of temperature gradient (except extending to higher wavenumbers) and approximately follows Kraichnan's universal form. The ratio of the eddy diffusivity of salt to that of heat is found to have an average slightly less than one. As discussed in the appendix, errors arise primarily from corrections for thermistor response and the shape of the scalar gradient spectrum at high wavenumbers; bias is also introduced due to anisotropy of weakly turbulent, buoyancy-influenced patches. As a result, the ratio $d_\chi = K_S/K_T$ is estimated to be $0.6 < d_\chi < 1.1$. While suggestive that $d_\chi < 1$, these results do not rule out the possibility that $K_S = K_T$. Consequences of this study are presented in section 6.

2. Methodology

a. Theory

1) SCALAR SPECTRA

We are concerned primarily with the dissipation range of turbulence, which contains most of the variance of gradient spectra (Nash and Moum 1999). Gradients of scalars are intensified and shifted to higher wavenumbers as a result of strain by the turbulent velocity field. This cascade of energy in the inertial subrange depends only on the dissipation rate of TKE, ϵ, leading to the classic $k^{-5/3}$ dependence of the velocity spectrum. Kolmogorov (1941) reasoned that viscosity only becomes important at wavenumbers of $O(k_\eta)$, where $k_\eta = (\epsilon/\nu^3)^{1/4}$. At higher wavenumbers, velocity fluctuations are heavily damped by molecular viscosity.

Since the values of the molecular diffusivities of heat D_T and salt D_S are much smaller than that for momen-

tum, fluctuations of T and S extend to much higher wavenumbers than fluctuations of velocity. Batchelor (1959) used this fact when he assumed that the evolution of scalars with $\mathrm{Pr} \equiv \nu/D_\theta \gg 1$ are governed solely by the mean least principal strain rate $\gamma \sim -(\epsilon/\nu)^{1/2}$, the strain associated with convergent motions in the turbulent velocity field.

A balance between the turbulence-induced strain and molecular diffusion occurs at a wavenumber near

$$\sqrt{\frac{|\gamma|}{D_\theta}} \sim \left(\frac{\epsilon}{\nu D_\theta^2}\right)^{1/4} \equiv k_b^\theta. \tag{4}$$

Batchelor (1959) calculated the spectral shape for scalar fluctuations in the viscous ranges. For the range of wavenumbers where molecular diffusion is not important ($k \ll k_b^\theta$), the spectrum of scalar gradient Ψ_{θ_z} may be written as (Corrsin 1951; Gibson and Schwarz 1963)

$$\Psi_{\theta_x}(k) = \frac{\chi_\theta}{|\gamma|} k. \tag{5}$$

This is referred to as the viscous–convective subrange. At the higher wavenumbers of the viscous–diffusive subrange, where molecular diffusion is important, Batchelor (1959) assumed that scalar fluctuations evolve in a spatially uniform field of strain and determined that the gradient spectrum roll off is proportional to e^{-k^2}. Kraichnan (1968) derived an alternate form for the theoretical spectrum by assuming a spatially intermittent strain field, which produces a less steep diffusive roll-off (proportional to e^{-k}). Although only subtly different at low wavenumbers, the peak of Kraichnan's form has less amplitude and is located at a lower wavenumber than that of Batchelor's form. Recent studies using direct numerical simulations have found the Kraichnan spectrum to be more representative of scalar variance spectra (Bogucki et al. 1997; Smyth 1999).

Assuming homogeneous, stationary, and isotropic turbulence, the dissipation rate of variance of a scalar θ is defined in terms of vertical gradients and the one-dimensional scalar spectrum

$$\chi_\theta = 6D_\theta \left\langle \left(\frac{\partial \theta}{\partial z}\right)^2 \right\rangle = 6D_\theta \int_0^\infty \Psi_{\theta_z}(k)\, dk. \tag{6}$$

While geophysical flows are generally considered isotropic in the dissipation subrange of turbulence (Smyth and Moum 2000), we address concerns about possible biases in estimating χ_S and χ_T from one-dimensional vertical gradient spectra in the appendix (sec. *e*).

2) Application to salinity

The following methodology differs slightly from that of Nash and Moum (1999) and Washburn et al. (1996), in which Ψ_{C_z} was interpreted in terms of the spectra Ψ_{S_z} and Ψ_{T_z}, and the T–S cross-spectrum $\Psi_{S_zT_z}$. Since $\Psi_{S_zT_z}$ cannot be directly measured, we instead determine

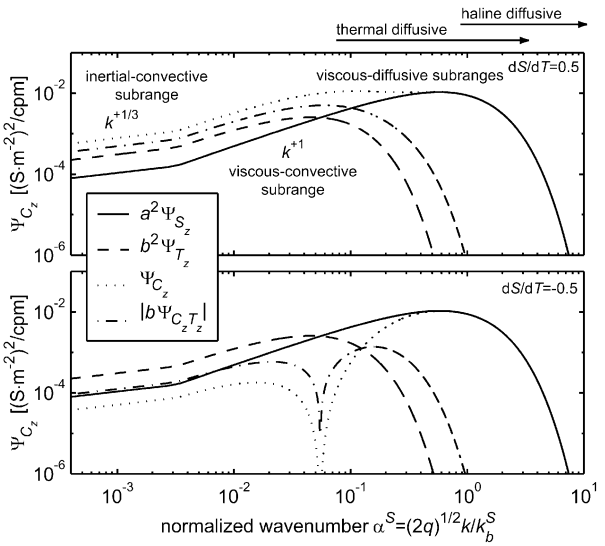

FIG. 1. Components of the salinity gradient spectrum Ψ_{S_z} for a theoretical turbulent patch. While each of the gradient spectra are necessarily positive, the cospectrum $\Psi_{C_zT_z}$ may take either sign depending on the local T–S relation. In the lower panel, for example, $dS/dT = -0.5$ psu K^{-1}, and as a result, $\Psi_{C_zT_z}$ is negative for large nondimensional wavenumbers ($\alpha^S > 5 \times 10^{-2}$). For this figure, it has been assumed that T and S are coherent and have constant phase at all wavenumbers.

the salinity spectrum Ψ_{S_z} explicitly in terms of T and C spectra and their cospectrum.

We begin by linearizing conductivity in terms of S and T:

$$C(T, S) = C_o + aS + bT, \tag{7}$$

where a and b are slowly varying functions of S, T, and P. For seawater at 35 psu and 10°C, $a \sim 0.097$ S m^{-1} psu^{-1} and $b \sim 0.095$ S m^{-1} K^{-1}. This indicates that a 1 K change in T has about the same effect on C as a 1 psu change in S. In addition, neither a nor b changes by more than 0.05% for a 1 psu change in S or a 1 K change in T, justifying this linearization. From Eq. (7) the vertical gradient in salinity ($\partial S/\partial z$) may be expressed in terms of the temperature and conductivity gradients ($\partial T/\partial z$, $\partial C/\partial z$):

$$\frac{\partial S}{\partial z} = \frac{1}{a}\frac{\partial C}{\partial z} - \frac{b}{a}\frac{\partial T}{\partial z}. \tag{8}$$

The gradient spectrum of salinity Ψ_{S_z} is then related to the gradient spectra of temperature Ψ_{T_z} and conductivity Ψ_{C_z} and the T–C gradient cospectrum $\Psi_{C_zT_z}$ as

$$\Psi_{S_z}(k) = \frac{1}{a^2}\Psi_{C_z}(k) - \frac{2b}{a^2}\Psi_{C_zT_z}(k) + \frac{b^2}{a^2}\Psi_{T_z}(k). \tag{9}$$

If measurements of T and C are fully resolved and collocated, then Ψ_{S_z} may be determined from three measurable spectra and χ_S calculated from Eq. (6). The theoretical form and wavenumber extent of each spectral component is shown in Fig. 1. Note that the sign of

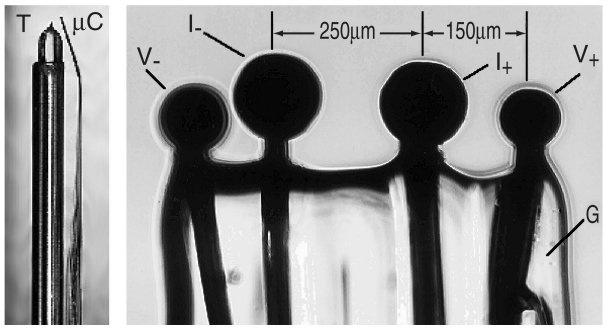

FIG. 2. A side view of the upper inch of the microconductivity–temperature (μCT) probe (left, 2 × mag). The fast-response FP07 microbead thermistor (T) is separated by 1 mm from the conductivity (μC) tip, a cross section of which is shown at right, magnified 100×. The conductivity probe consists of two current-supplying (I_-, I_+) and two voltage-measuring spherical platinum electrodes (V_-, V_+) supported by a fused glass matrix (G). The sensor averages conductivity over a bipolar volume of radial extent ~3 mm and has a −3 dB power attenuation near $k \sim 300$ cpm. (Photographs courtesy Mike Head, Precision Measurement Engineering.)

$\Psi_{C_zT_z}$ cannot be guaranteed, and depends on the slope of the local *T–S* relation.

b. Experimental details

To calculate Ψ_{S_z}, all of Ψ_{T_z}, Ψ_{C_z}, and $\Psi_{C_zT_z}$ must be fully resolved. This requires a fast-response sensor that measures *T* and *C* at the same location. The microconductivity–temperature (μCT) probe (manufactured as the fast conductivity and temperature probe by Precision Measurement Engineering; Head 1983) is one such sensor (Fig. 2). The probe consists of a four-electrode conductivity sensor (μC) separated by 1–2 mm from a Thermometrics' FP07 fast-response microbead thermistor. The conductivity measurement averages over an ~$(3\ \text{mm})^3$ volume and its response is wavenumber-limited (3 dB attenuation at 300 cpm; see appendix of Nash and Moum 1999). The FP07 response is limited by the rate of heat transfer into the thermistor bead (through the hydrodynamic boundary layer and glass coating), which translates to a frequency-limited response (double pole with $f_c = 29$ Hz for the thermistors used here; see Nash et al. 1999). The response function for the thermistor was calculated by comparing spectral amplitudes of the FP07 to that of our ultrafast-response thermocouple sensor and to the μC sensor for selected patches where salinity fluctuations were negligible (see appendix, sec. *a*). Such spectral corrections extend the useful range of the FP07 to ~60 Hz.

The μCT probe was installed on Chameleon, our loosely tethered microstructure profiler, in addition to the regular suite of microstructure sensors: a pitot tube used to measure the fluctuating vertical velocity and estimate $\langle w'T' \rangle$, $\langle w'S' \rangle$, and $\langle w'^2 \rangle$ (Moum 1990); airfoil shear probes used to estimate ϵ, the dissipation rate of TKE (Moum et al. 1995, e.g.); a second fast-response FP07 thermistor; and a stable Neil-Brown conductivity cell, used to calibrate the μC sensor in situ. Casts using the ship's SeaBird CTD were periodically made for comparison with Chameleon's temperature and conductivity measurements.

Because the μCT probe is designed for laboratory use, it is susceptible to fouling and damage, and it is difficult to obtain a stable laboratory calibration. As a result, we calibrate the sensor in situ: polynomial calibration coefficients are determined by fitting a low-pass filtered μC signal to the conductivity measured by the Neil-Brown cell. The coefficients obtained are then applied to the unfiltered μC signal and its derivative. Care is taken not to include μC data that contain nonphysical spikes or steplike features, which are not present in the conductivity time series from the Neil-Brown cell and likely represent an impact of the sensor with biology. After patches are selected, the μC and Neil-Brown signals are again compared; records which differ significantly are discarded.

The μC sensor was sampled at 409.6 Hz and its derivative at either 819.2 or 409.6 Hz, depending on the experiment. Thermistor temperature and its derivative were sampled at 102.4 and 204.8 Hz, respectively. Four-pole analog Butterworth filters were used for antialiasing before digitizing at 16 bits; filter cutoff frequencies of 32, 64, 132, and 245 Hz were used for signals sampled at 102.4, 204.8, 409.6, and 819.2 Hz, respectively. The transfer functions of the filters and analog differentiators were determined in the laboratory and spectral corrections to restore lost variance were applied to the data during processing.

To measure 80% of the variance of Ψ_{T_z} and Ψ_{S_z} in an energetic turbulent patch ($\epsilon = 1 \times 10^{-6}\ \text{m}^2\ \text{s}^{-1}$, e.g.), the μCT probe must resolve dT'/dz from 0 to 200 cpm and dC'/dz from 0 to 2000 cpm. In an attempt to achieve this, an instrument profiling speed of $W_o = 25$–$35\ \text{cm s}^{-1}$ was selected by adjusting the buoyancy and drag elements on Chameleon. As a result, the average resolved wavenumber during the experiment was 215 cpm for dT'/dz and 710 cpm for dC'/dz. This choice of fall speed was a compromise between adequately resolving the scalar spectra while still allowing Taylor's frozen-flow hypothesis to be invoked (permitting the conversion of temporal to spatial derivatives; i.e., $W_o^{-1}d/dt \rightarrow d/dz$). Sensitivity of the shear probes and the pitot tube is high at these profiling speeds.

Several hundred vertical profiles (from the surface to the bottom at depth 50–200 m) were acquired on two separate occasions on Oregon's continental shelf on the southern flanks of Heceta Bank on 23 August 1998 and over Stonewall Bank on 15 April 1999. Measurements of turbulent vertical velocity w' were obtained only during the Heceta Bank experiment. During the Stonewall Bank experiment, a third temperature sensor (an ultrafast-response thermocouple: Nash et al. 1999) was installed on Chameleon and used as a benchmark to determine the thermistor frequency-response transfer function in situ.

The dominant currents at Heceta Bank follow local isobaths. Near the crest of the bank, the flow is mostly to the southeast and mixing is dominated by bottom-boundary processes. Offshore of the bank, the southeast flowing surface currents are opposed by a northwestward flowing undercurrent, which combine to produce an intensified shear region near depth 70 m. The stratification near the surface is mostly due to temperature; at depth, where temperature inversions and salinity intrusions are common, salinity plays a more dominant role.

At Stonewall Bank, currents were dominated by a strong southwestward (>0.5 m s^{-1}) internal hydraulic flow (Moum and Nash 2000; Nash and Moum 2001). This flow produced interfacial shear instabilities between a plunging lower layer and the near-stagnant upper layer; intensified bottom boundary mixing and hydraulic jumps were also observed. Between the two experiments, a wide variety of *T–S* relations was observed at a range of turbulence intensities.

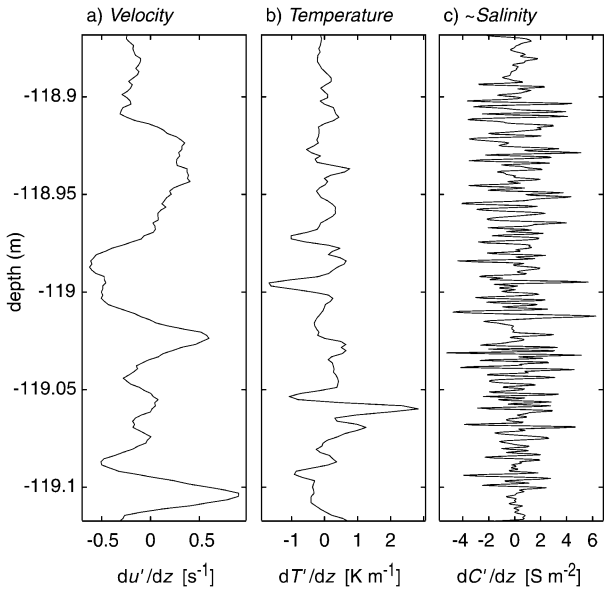

FIG. 3. A 25-cm vertical segment of (a) du'/dz, (b) dT'/dz, and (c) dC'/dz within a turbulent patch at depth 120 m near Heceta Bank. The spatial scales of conductivity gradient are dominated by the salinity gradient and are ~10 times smaller than those of temperature gradient, as indicated by the number of zero crossings in a given spatial interval, and is consistent with $k_b^s/k_b^T \sim 10$. The scales of du'/dz are larger than either dT'/dz or dC'/dz.

1) PATCH SELECTION

Single spectra of turbulence tend to be highly variable; in order to produce significant results, spectra must be ensemble-averaged to reduce the uncertainty and natural variability of the individual spectral estimates. Averaging is even more important to reduce the variability of composite spectra, which may rely on the difference between two spectral components of similar magnitudes. To increase the degrees of freedom of spectral estimates, the components Ψ_{T_z}, Ψ_{C_z}, and $\Psi_{C_zT_z}$ were ensemble averaged within a homogeneous region before combining to form Ψ_{S_z}.

Turbulent patches were selected with regard to homogeneity of du'/dz, dC'/dz, and dT'/dz signals and uniformity of the mean gradient dS/dT. The *T–S* relation was required to be linear so that the relative contributions of T' and S' to C' would remain constant. To illustrate how Ψ_{S_z} and χ_S are calculated, data from a sample patch are shown in Fig. 3 (time–spatial series) and Fig. 4 (spectra).

Figure 3 illustrates the range of the spatial scales of the smallest velocity, temperature, and salinity fluctuations. For this patch, dC'/dz approximately represents dS'/dz, because the contribution of salinity gradient to conductivity gradient is much greater than that of temperature gradient. Note that the turbulent signal of dC'/dz in Fig. 3c is contained within the 20-cm band between 118.9 and 119.1 m; the lack of strong fluctuations outside this region indicates that the signal-to-noise ratio is high within the 20 cm layer.

2) ESTIMATING SCALAR DISSIPATION RATES FROM SPECTRA

If scalar spectra are fully resolved, then χ_θ is simply the complete integral of Eq. (6). In practice, measurements are limited by sensor response or noise at the smallest scales (or highest frequencies) and prevent complete integration of the scalar gradient spectrum. We define $k^\theta_{\max}$ as the maximum wavenumber at which spectral estimates are resolved and unaffected by noise. The choice of $k^\theta_{\max}$ depends on the magnitude of ϵ and χ relative to the sensor noise; for the purposes of this analysis, we have found it prudent to select $k^\theta_{\max}$ by hand.[1] At wavenumbers near $k^\theta_{\max}$, spectral levels may be contaminated by sensor noise; the effect of this contamination on biasing χ_T is discussed in the appendix (sec. *b*) and found to be negligible.

A discussion of the frequency response of the microbead thermistor is given in Nash et al. (1999) and in the appendix (sec. *a*). The spatial response of the μC sensor is described in Nash and Moum (1999). For each of these sensors, corrections are applied in the frequency–wavenumber domain in order to restore lost variance. In addition, corrections were applied to account for the antialiasing filters and the imperfect response of the analog differentiators. Error and bias associated with the response corrections are discussed in the appendix (sec. *a*).

In practice we determine χ_θ by integrating $\Psi_{\theta_z}(k)$ over the subrange $0 < k < k^\theta_{\max}$. In order to account for variance not resolved by the probe, we assume a uni-

[1] Here $k^\theta_{\max}$ is selected as the wavenumber where a given spectrum intersects the noise continuum, defined from spectra where the turbulence signal is weak.

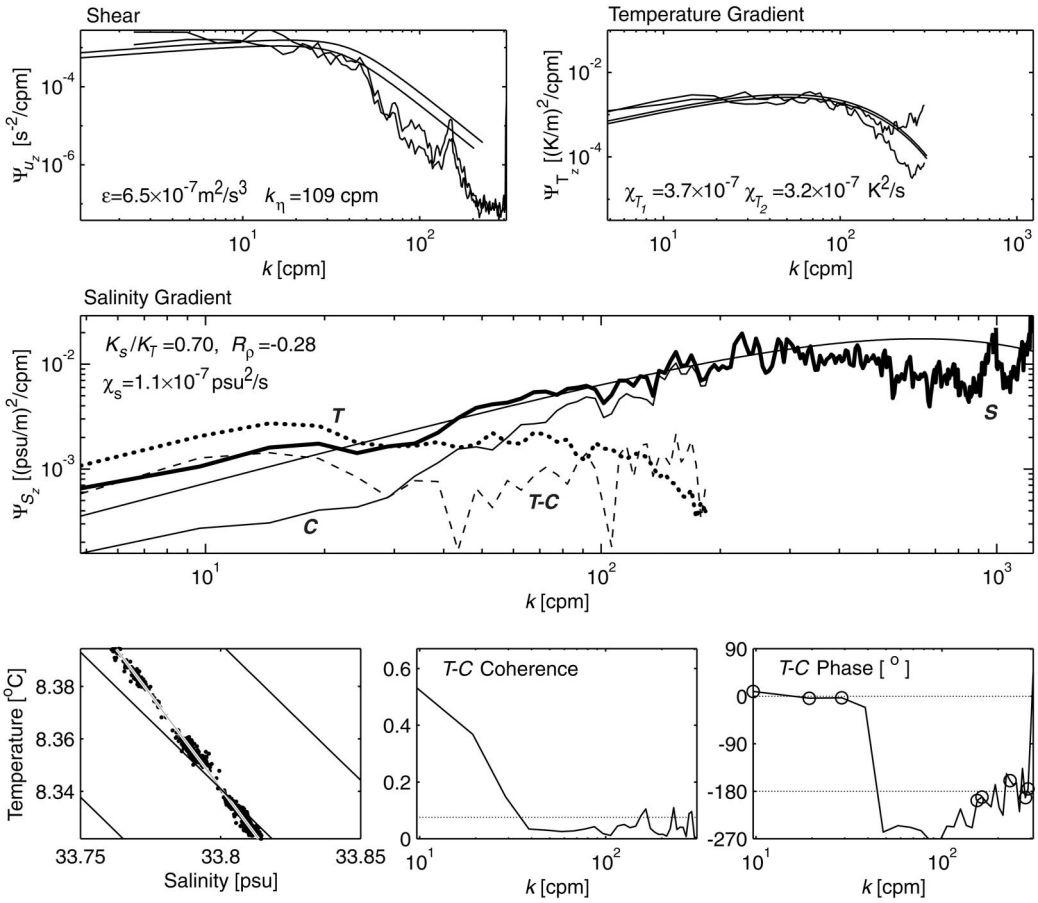

FIG. 4. Gradient spectra of velocity, temperature, and salinity associated with a turbulent patch 3-m-thick (the data shown in Fig. 3 is contained within this patch). Smooth curves represent the universal forms of Nasmyth (for shear spectra) and Kraichnan (for scalar gradient spectra). The upper-left panel shows the two orthogonal components of velocity shear Ψ_{u_z}, Ψ_{v_z}. Temperature gradient spectra Ψ_{T_z} from two thermistors (upper right) indicate that the high-frequency noise from one probe (that on the μCT probe used in this analysis) is significantly less than the other. In the center panel, the components of the composite salinity gradient spectrum Ψ_{S_z} (thick solid line) are shown in units of salinity gradient: the contribution from C, $a^{-2}\Psi_{C_z}$ (thin solid line); the contribution from T, $a^{-2}b^2\Psi_{T_z}$ (dotted); and that from the cospectrum, $|2a^{-2}b\Psi_{C_zT_z}|$ (dashed). Note that the cospectrum is positive at low wavenumbers and negative at high-k, as shown in the plot of T–C phase (lower right; circles indicate significant phase). The T–C coherence is shown in the lower middle panel, with the 95% significance level indicated (dotted line). The T–S relation is shown to the lower left; this represents a type C patch, as described in section 3b.

versal form for the scalar spectrum at unresolved wavenumbers; the variance contained in the measured $[\Psi_{\theta_z}(k)]_{\text{obs}}$ and theoretical $[\Psi_{\theta_z}(k)]_{\text{theory}}$ spectra at resolved wavenumbers is assumed to be equal.[2]

$$\int_{k^\theta_{\min}}^{k^\theta_{\max}} [\Psi_{\theta_z}(k)]_{\text{obs}}\, dk = \int_{k^\theta_{\min}}^{k^\theta_{\max}} [\Psi_{\theta_z}(k)]_{\text{theory}}\, dk. \quad (10)$$

Two different forms of the theoretical scalar spectra are used for the above integration correction: that by Batchelor (1959) and Kraichnan (1968). The wavenumber extent of the theoretical scalar gradient spectrum depends on ϵ (determined from two independent shear probe estimates) and the value of the universal constant q. The effect of the value of q on our estimates is explored in the appendix (sec. *f*).

We remove the dependence of the theoretical shape on q by forming the nondimensional wavenumber $\alpha^\theta = \sqrt{2q}(k/k^\theta_b)$. For our well-resolved temperature gradient spectra, the method of Luketina and Imberger (2001) can be adapted to determine $k^T_b/\sqrt{2q}$. This method minimizes the error between the theoretical and observed scalar spectra while constraining the total variance of the theoretical form to be that of the data.[3] Using the

[2] One-dimensional spectra are calculated by dividing the patches into ~0.5 m, 50% overlapped segments that are Hanning windowed, Fourier transformed, and ensemble averaged. Frequencies are converted to wavenumber using Taylor's hypothesis: $k = f/W_o$.

[3] This method is typically used to estimate ϵ from slowly profiling

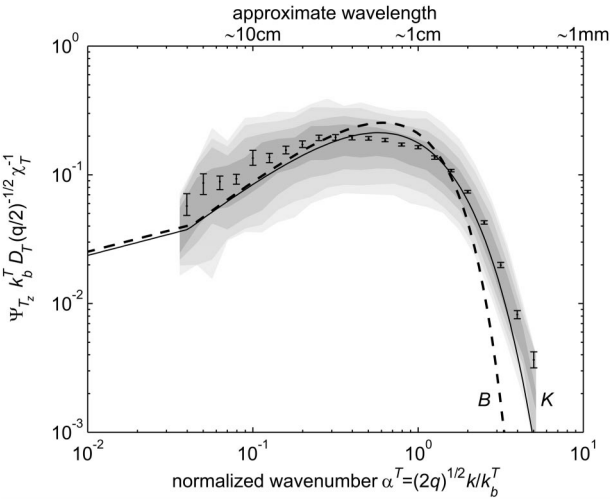

FIG. 5. Summary of 407 nondimensionalized spectra of temperature gradient as a function of temperature-normalized wavenumber $\alpha^T = \sqrt{2q}(k/k_b^T)$. Error bars represent 95% bootstrap confidence intervals on the mean. The distribution of spectral estimates is indicated by shading: progressively darker regions contain 95%, 90%, 75%, and 50% of the spectral estimates in a given wavenumber band (5×10^4 estimates in total; each contains a minimum of 50 degrees of freedom). The smooth lines represent the theoretical spectral shapes of Batchelor (dashed) and Kraichnan (solid). Most temperature gradient spectra are resolved to $\alpha^T = 4$; all are resolved at $\alpha^T = 2$. The approximate dimensional wavelength is indicated above the figure; these values are within a factor of 2 of the actual wavelengths.

Kraichnan universal form as a benchmark, this comparison indicates that q_k is variable and averages ~7.5 (see Fig. A7).

3. Observations

a. Temperature gradient spectra

To estimate χ_S, temperature fluctuations must be resolved in order to remove the contribution of Ψ_{T_z} from Ψ_{C_z} to form Ψ_{S_z} through Eq. (9). Nondimensionalized spectra of temperature gradient are shown in Fig. 5. To avoid bias in the spectral estimates in the viscous–diffusive subrange, the value of q is calculated following the method of Luketina and Imberger (2001) and is determined individually for each patch. Such a normalization by $k_b^T/\sqrt{2q}$, which depends only on the wavenumber extent of Ψ_{T_z} and not on an independent measure of ϵ, collapses spectral estimates to a universal form at high wavenumbers. This is because the variability in q (discussed in the appendix, sec. *f*) is accounted for. Otherwise, in regions where the spectrum decreases rapidly with wavenumber, uncertainty introduced into the wavenumber normalization (through variability in the relationship between ϵ and Ψ_{T_z}) increases the spread in spectral estimates and biases the ensemble-average high.

Spectra of temperature gradient closely follow the theoretical shape of Kraichnan (1968) especially near $\alpha^T \sim 1$, the scales which contain most of the gradient variance. At the lower wavenumbers of the convective–diffusive subrange ($\alpha^T \sim 0.1$), spectral amplitudes are significantly greater than those predicted by either the Batchelor or Kraichnan forms. Many investigators have observed a deviation in the convective–diffusive subrange, which may be attributed to remnant background vertical temperature structure. Dillon and Caldwell (1980) found that the deviation is greatest for small Cox numbers ($C_x^T = \langle (dT'/dz)^2 \rangle / \langle dT/dz \rangle^2$) and that observed spectra approach the theoretical form for $C_x^T > 2500$. However, this deviation may also result if a small fraction of variance near the spectral peak cascades to lower wavenumbers in a *reverse cascade* (discussed further in section 4d.)

b. T–C cospectrum, coherence, and phase

The collapse of the normalized temperature gradient spectrum to Kraichnan's theoretical form gives us confidence that our temperature measurements are fully resolved. We will proceed to calculate the salinity gradient spectrum, which, using Eq. (9), depends on both Ψ_{T_z} and $\Psi_{C_zT_z}$. Since Ψ_{T_z} is fully resolved, we assume that $\Psi_{C_zT_z}$ is also resolved because the cospectrum extends to wavenumbers < 1.5 times that of temperature in the extreme case of perfect *T–C* correlation.

The cospectrum $\Psi_{C_zT_z}$ is not strictly positive nor is the cross-spectrum, in general, real; both depend on the local *T–S* relation. However, if *T* and *S* are highly correlated, as we would expect (at least at the largest scales) from a turbulent overturn, then the phase between *T* and *C* approaches the limiting values of $\phi = 0°$ or $\phi = 180°$ at low wavenumbers. We use the *T–S* diagram in Fig. 6 to illustrate three distinct cases. A summary of the average phase and coherence of our observations is shown in Fig. 7 for three different ranges of the density ratio

$$R_\rho = -\frac{\alpha_o}{\beta_o}\frac{dT/dz}{dS/dz},$$

where α_o is the thermal expansion coefficient and β_o is the haline contraction coefficient. Here T_z and S_z are found to be either in phase or out of phase, with $\alpha \sim 20°$ spread in the distribution. Note that $R_\rho = -0.22$ represents a line of constant conductivity.

Case A: T', C', and S' are in phase. The fluctuations in T' and S' are positively correlated on large scales, so that positive fluctuations occur simultaneously in both T' and S' and give rise to a positive fluctuation in C'. Even as T' is attenuated at high wavenumbers (near $k \sim k_b^T$), T' and C' remain positively correlated. This results because C' is dominated by S' at wavenumbers $k > k_b^T$ so that S' and C' are both positively correlated

devices without shear probes if one assumes a fully resolved temperature gradient spectrum and constant value for *q*.

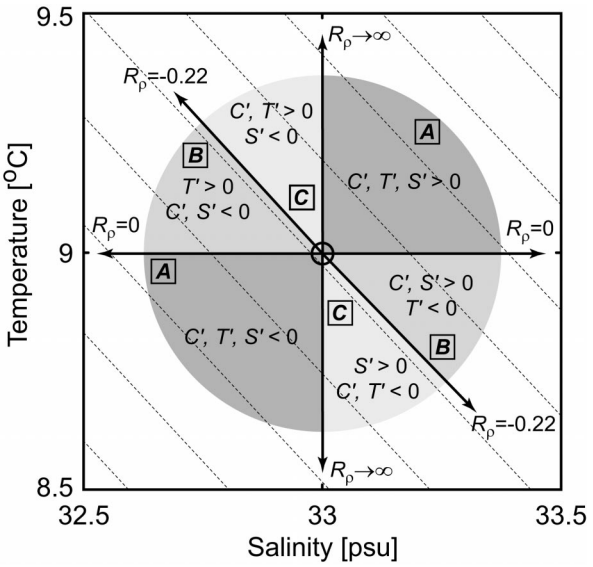

FIG. 6. An aid to understanding *T*–*C* phase and coherence. Indicated on a *T*–*S* diagram are lines of constant conductivity (dotted) and three distinct regions (shaded) with *T*–*S* slopes that give rise to different *T*–*C* phase. The segments of the circle represent regions in *T*–*S* space where turbulent fluctuations (T', S', and C' relative to the origin, 33 psu, 9°C) could occupy. The large-scale turbulent fluctuations represented on this diagram are generally aligned with the slope of the local *T*–*S* relation and form a line segment passing through the origin. Each of the three regions (***A***, ***B***, and ***C***) are discussed in detail in the text.

with T'. This gives rise to the high *T*–*C* coherence and zero phase in Fig. 7 (case **A**).

Case B: T' is out of phase with both C' and S'. This is the case where salinity dominates the conductivity signal on the overturning scale. Since T' becomes attenuated at higher wavenumbers, S' must also dominate C' at the smallest scales. Hence, as long as T' and S' remain anticorrelated, T' and C' should also remain anticorrelated, as shown in Fig. 7 (case **B**). Note that the coherence is much lower for case **B** than for case **A**. This is an indication that T' and S' are, in fact, decorrelating from each other at scales near $\sim 0.2k_B^T$. For case **A**, the coherence represents that between T' and a possibly temperature-dominated C'; for case **B**, the coherence represents that between T' and a salinity-dominated C', and is decreased due to a decrease in *T*–*S* coherence.

Case C: S' is out of phase with both C' and T' on large scales. Conductivity is dominated by temperature on the energy-containing scales. However, above the thermal–diffusive wavenumbers (near $\sim 0.5k_B^T$), T' is attenuated and S' dominates C'. Since S' is anticorrelated with T', C' is also anticorrelated with T' at the smallest scales. Hence the phase changes from 0° to 180° in many spectra at the location where C' undergoes a transition between T' dominance and S' dominance, as shown in Fig. 7 (case **C**). The sample patch in Figs. 3 and 4 has *T*–*S* characteristics corresponding to case **C**.

The cospectrum $\Psi_{C_z T_z}$ may therefore represent ether a positive or negative contribution to Ψ_{S_z} in Eq. (9), depending on the *C*–*T* phase. The value of R_ρ therefore helps to determine the shape of the *T*–*C* cospectrum and its contribution to Ψ_{S_z}.

c. Salinity gradient spectra and dissipation

In the previous sections, we identified and characterized the components of Ψ_{C_z} that result from temperature microstructure. In this section, we remove those contributions in order to estimate Ψ_{S_z}.

The nondimensionalized spectrum of salinity gradi-

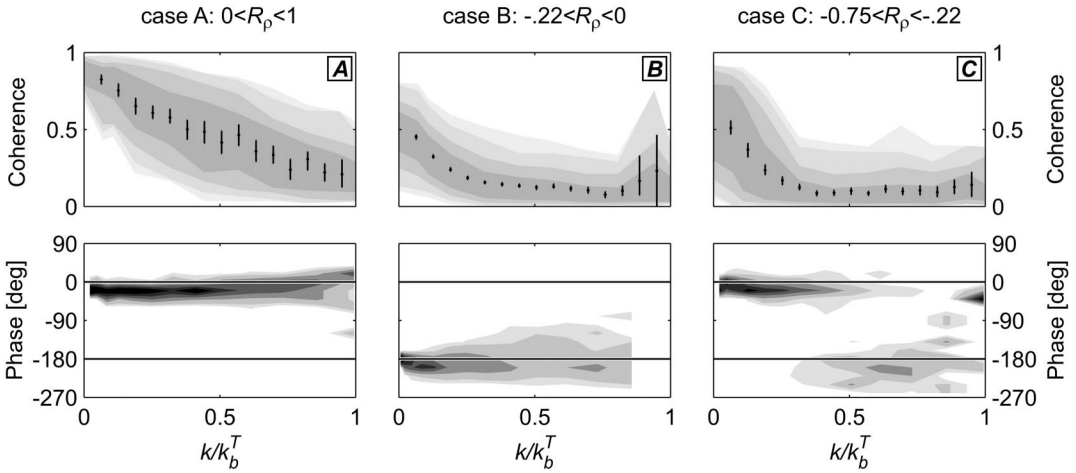

FIG. 7. Shading indicates the distribution of coherence (top) and phase (bottom) between dT'/dz and dC'/dz; error bars represent 95% bootstrap confidence intervals. Patches have been averaged over the three different ranges of R_ρ identified in Fig. 6 which characterize the distinct trends in phase and coherence described in the text. The phase has been plotted only for estimates where the coherence is significant; the average significance level is 0.15, and varies with patch length.

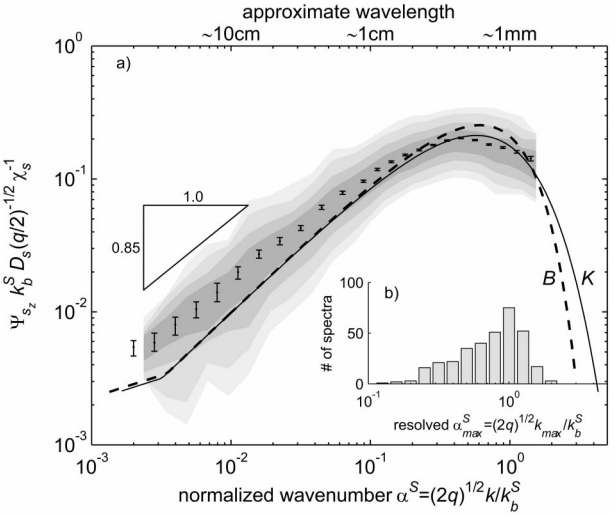

FIG. 8. Summary of 350 nondimensionalized spectra of salinity gradient as a function of salinity-normalized wavenumber $\alpha^S = \sqrt{2q}(k/k_b^S)$ (a). Error bars represent 95% bootstrap confidence intervals on the mean; the shading indicates the distribution of spectral estimates. The smooth lines represent the theoretical spectral shapes of Batchelor (dashed) and Kraichnan (solid). A histogram of the resolved wavenumber k_{max} (which represents the Nyquist wavenumber or the wavenumber at which each spectrum was truncated because of noise) is shown in the inset (b); wavenumber is scaled to match that of the larger figure. Only patches with $|R_\rho| < 1$ were used for this analysis.

ent, shown in Fig. 8, approximately follows the universal form of Kraichnan. Only spectra with $|R_\rho| < 1$ were used in this analysis (350 patches). These represent patches where the temperature contribution is less than 20 times the salinity contribution to the conductivity gradient spectrum. For $|R_\rho| > 1$, the contribution of Ψ_{T_z} to Ψ_{C_z} is overwhelming: the conductivity gradient spectrum is 95% due to temperature gradient at low wavenumbers. Because Ψ_{S_z} is the difference between $(\Psi_{C_z} + b^2\Psi_{T_z})$ and $2b\Psi_{C_zT_z}$ [Eq. (9)] and these terms are of similar magnitude for $|R_\rho| > 1$, spectral variability and relatively small errors in either Ψ_{T_z}, Ψ_{C_z}, or $\Psi_{C_zT_z}$ can lead to a large relative error in Ψ_{S_z}.

In light of this, it is remarkable that the spectral estimates in Fig. 8 have such a narrow spread, given that a significant temperature contribution has been removed from Ψ_{C_z} to produce these spectra. This is testimony that the linear decomposition of conductivity spectra [Eq. (9)] provides an excellent model for interpreting our observations. We attribute the spread in spectral estimates, which is similar for Ψ_{S_z} and Ψ_{T_z}, to natural variability and conclude that the error associated with Ψ_{S_z} being a composite spectrum is small in comparison. As indicated in the figure, the slope in the viscous–convective subrange is less that $+1$.

The dissipation of salinity variance χ_S is calculated by integrating Ψ_{S_z} using Eq. (6). Since it is often assumed (Gregg 1984) that χ_S and χ_T are simply related through the square of the *T*–*S* slope, $(dS/dT)^2$ [Eq. (2)],

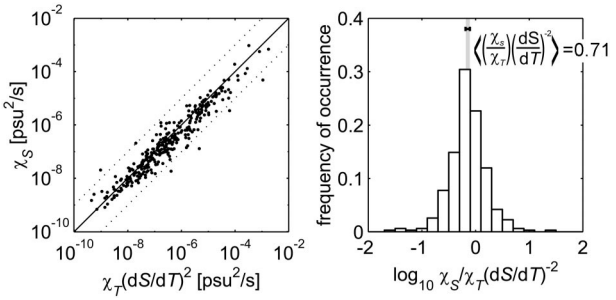

FIG. 9. Comparison of the direct estimate of salinity variance dissipation χ_S with its proxy formed from χ_T and the square of the mean *T*–*S* gradient $(dS/dT)^2$.

we present a comparison with this form in Fig. 9. These results indicate that $\chi_T(dS/dT)^2$ is an excellent proxy for χ_S, with the latter being on average about 30% less than the former. This difference might be a real effect of differential turbulent diffusion. However, it may also result from error and bias in our experimental determination of χ_T and χ_S. Uncertainty in the thermistor response transfer function, the assumed shape of the universal spectrum used for integration correction, and the use of the isotropic relations in estimating scalar dissipations represent the largest sources of error and can account for the observed 30% discrepancy between $\chi_T(dS/dT)^2$ and χ_S (see appendix).

d. Covariance flux estimates

A fundamental motivation for studying the mixing of scalars is to determine turbulent fluxes (Gregg 1987). The covariance (or eddy correlation) estimate of the turbulent vertical flux for a scalar θ in Eq. (1) is given by the covariance

$$F^\theta = \langle w'\theta' \rangle, \tag{11}$$

where w' represents the fluctuating vertical velocity (from our pitot measurements: Moum 1996a,b) and θ' is the associated scalar fluctuation with respect to the background scalar profile $\overline{\theta}$. The background is often defined by resorting the observed density ρ to its lowest potential energy (*Thorpe reordered*) state. However, if both *T* and *S* contribute to ρ, a Thorpe reordered profile often contains spikes and discontinuities in *T* of *S* due to small errors in computing density from two independent measurements. Since the patches used in this analysis have an approximately linear *T*–*S* relation, the lowest potential energy state should be monotonically increasing (or decreasing) in all $T(z)$, $S(z)$, and $\rho(z)$. To produce such a background state, we find it most appropriate to sort *T* and *S* individually to determine $\overline{T}$ and $\overline{S}$. We then compute density ρ_{TS} from the reordered $\overline{T}$, $\overline{S}$ profiles and compare it to the Thorpe reordered density profile ρ_{Thorpe}. If the normalized deviation $\langle(\rho_{TS} - \rho_{\text{Thorpe}})^2\rangle/(\rho_{\text{Thorpe}} - \overline{\rho})^2$ exceeds 0.002 for a given turbulent patch, then this method of sorting is deemed inadequate and the scalar

fluctuations and corresponding turbulent fluxes $\langle w'\theta'\rangle$ are not computed. If the normalized deviation is small, ρ_{TS} closely matches ρ_{Thorpe} and the associated $\overline{T}$ and $\overline{S}$ are smooth. A sample patch is shown in Fig. 10.

In Eq. (11), the angle brackets should ideally represent an average over the full spatial extent and temporal lifespan of a turbulent event. In practice, this is not possible from vertical-profiler measurements, and instead the averaging is performed with respect to a single dimension (z) instead of four (x, y, z; t). As a result of this undersampling, single-patch estimates of $\langle w'\theta'\rangle$ are highly variable and may even be countergradient (Moum 1996a,b). Estimates of F^{θ} are thus only reliable when ensemble averaged over many turbulent events.

It was possible to unambiguously determine the background $\overline{T}$, $\overline{S}$ in 176 of the 233 turbulent patches in which w' was measured. Only 129 had $|R_\rho| < 1$, a condition necessary if comparisons with K_S are to be made. In addition, it is necessary for the coherence between w' and θ' to be significant to calculate the covariance. Only 76 patches were significant in both $\langle w'T'\rangle$ and $\langle w'S'\rangle$ at the 95% level.

4. Discussion

a. Universality of spectral shape

A comparison of the gradient spectra of T and S is shown in Fig. 11 as a summary. Two different normalizations illustrate the similarities and differences in the two spectral shapes. In Fig. 11a, the data are normalized using Kolmogorov scaling so that spectra collapse at the wavenumbers associated with the maximum variance in the velocity strain field (near k_η). The scale separation between inertial subrange and diffusive (Batchelor) scales is 10 times greater for Ψ_{S_z} than for Ψ_{T_z}, allowing a large viscous–convective subrange to develop.

In Fig. 11b, the data are normalized using Batchelor scaling so that spectra collapse in the viscous–diffusive subrange: Ψ_{T_z} and Ψ_{S_z} have a similar shape and approximately follow the universal form of Kraichnan. While Ψ_{T_z} extends to higher normalized wavenumbers (due to the thermistor's comparatively high signal-to-noise ratio), the spectrum of salinity gradient extends to lower normalized wavenumbers, indicating that the scales of its diffusive subrange are further removed from the scales of the velocity strain field, and Ψ_{S_z} should be less affected by larger scale, buoyancy-modified variance and are likely more isotropic (see the appendix, sec. *e*.)

In the region where Ψ_{T_z} and Ψ_{S_z} overlap in Fig. 11b, the shapes of the spectra are remarkably similar to each other, yet different from the universal form of Batchelor. This provides further support to the recent acceptance of Kraichnan's universal form (see Smyth 1999; Bog-

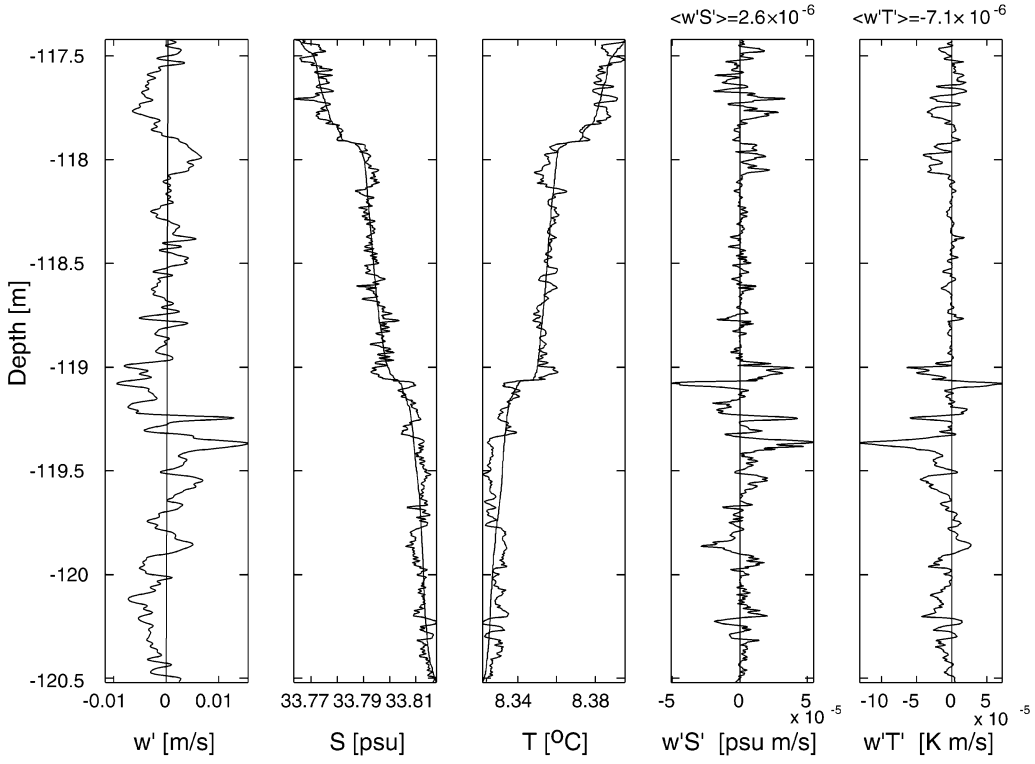

FIG. 10. Turbulent vertical velocity w' (left) and the associated instantaneous turbulent fluxes, $w'S'$ and $w'T'$ (right panels) for the patch shown in Fig. 4. Also shown are S and T along with the associated resorted profiles. On average, positive w' is associated with positive S' and negative T', leading to the downgradient fluxes of heat ($\langle w'T'\rangle = -7.1 \times 10^{-6}$ K m s^{-1}) and salt ($\langle w'S'\rangle = 2.6 \times 10^{-6}$ psu m s^{-1}).

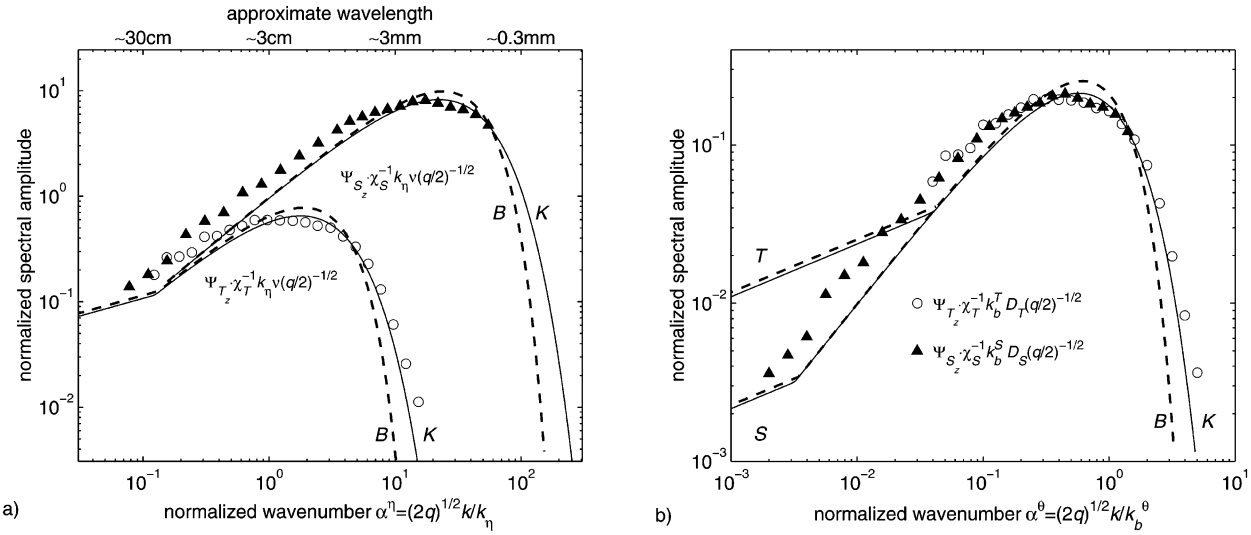

FIG. 11. Collapse of salinity (▲) and temperature (○) gradient spectra in the viscous–convective (a) and viscous–diffusive (b) subranges is accomplished by appropriate normalization. In (a) both Ψ_{S_z} and Ψ_{T_z} are nondimensionalized with respect to the Kolmogorov wavenumber k_η and molecular viscosity ν, which collapses the low-wavenumber inertial and viscous–convective subranges. In (b) Ψ_{S_z} and Ψ_{T_z} are nondimensionalized by their respective Batchelor wavenumbers (k_b^S or k_b^T) and molecular diffusivities (D_S or D_T), which collapses the spectra in the high-wavenumber viscous–diffusive subrange. The dashed and solid curves represent the universal forms of Batchelor and Kraichnan. Note that the $k^{1/3}$ inertial subrange has a different level and transition wavenumber for each scalar under the latter normalization.

ucki et al. 1997, e.g.), which more accurately represents the spectral shape in the viscous–diffusive subrange by allowing intermittency in the strain field.

In the viscous–convective subrange, spectral amplitudes are elevated over either universal shape so that the spectral slope in the viscous–convective subrange is less than +1. There are two possible reasons for this:

- increased spectral intensity at low wavenumbers, as a result of the background vertical salinity structure [as has been suggested for T by Dillon and Caldwell (1980) and others] or
- salinity variance within the viscous–convective subrange may return to larger wavenumbers in a *reverse cascade*, a result of incomplete mixing.

The latter is consistent with $d_\chi = K_S/K_T < 1$, and will be discussed in more detail in section 4d.

b. Flux comparisons

Following Gargett and Moum (1995), we define the turbulent flux of a scalar θ in three ways:

1) based on the direct flux from covariance estimates,

$$F^\theta \equiv \langle w'\theta' \rangle \tag{12}$$

2) relating shear production to buoyancy production plus dissipation in the evolution equation of TKE,

$$F_\epsilon^\theta \equiv \epsilon \frac{\theta_z}{N^2} \tag{13}$$

3) from the $P_\theta = \chi_\theta$ balance in the scalar variance equation [Eq. (1)],

$$F_\chi^\theta \equiv \frac{\chi_\theta}{2\theta_z}. \tag{14}$$

The corresponding flux coefficients are

$$\Gamma_o^\theta = F^\theta/F_\epsilon^\theta, \qquad \Gamma_d^\theta = F_\chi^\theta/F_\epsilon^\theta. \tag{15}$$

The statistics of Γ_d^θ are shown in Fig. 12. The mean $\langle\Gamma_d^T\rangle = 0.11$ is consistent with observations of oceanic microstructure and laboratory experiments: $\langle\Gamma_d^S\rangle$ has never been measured before and we find it to be about 30% less than $\langle\Gamma_d^T\rangle$.

Our estimates of Γ_o^θ (Fig. 13) are similar for salinity and temperature, but are perhaps a factor of 2 smaller than would be expected. Our measurements of w appear not to resolve the largest scales at which the eddy flux occurs. Regardless, $\langle\Gamma_o^T\rangle \sim \langle\Gamma_o^S\rangle$, indicating that heat and salt are transported equally well by the eddies that are resolved.

For high Re_b flows ($\mathrm{Re}_b \equiv \epsilon/(\nu N^2)$), the relative turbulent fluxes of heat and salt should be proportional to the ratio of their mean gradients [refer to Eq. (13) for example]. We define the dissipation diffusivity ratio d_χ following Gargett and Holloway (1992) and introduce the covariance diffusivity ratio d_o:

$$d_\chi = (F_\chi^S/F_\chi^T)(dT/dS), \qquad d_o = (F_o^S/F_o^T)(dT/dS); \tag{16}$$

d_χ is equivalent to the ratio of diffusivities K_S/K_T. Departures of d_χ from 1 represent differences in the effectiveness of turbulence in diffusing salt relative to heat at the diffusive scales. In contrast, d_o represents the differential diffusion of S with respect to T on the eddy-flux scales. The statistics of these two ratios are shown

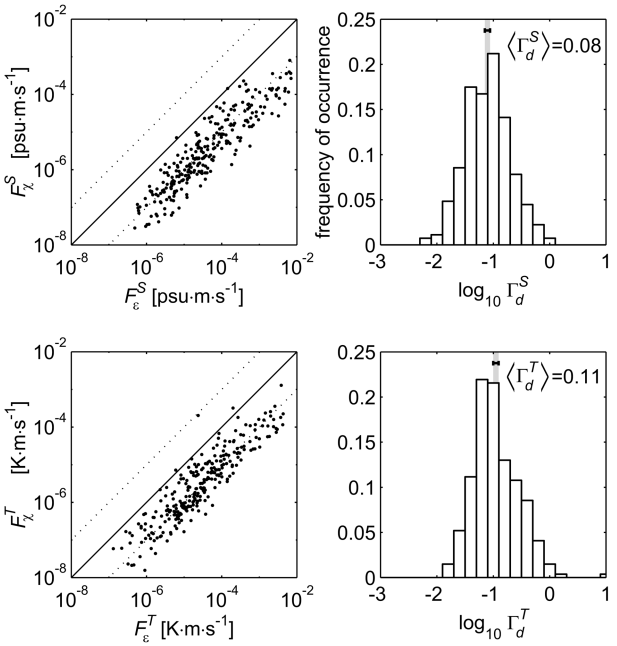

FIG. 12. Statistics of Γ_d, the dissipation flux coefficient based on the irreversible mixing on diffusive scales. Estimates were made from 350 patches with $|R_\rho| < 1$.

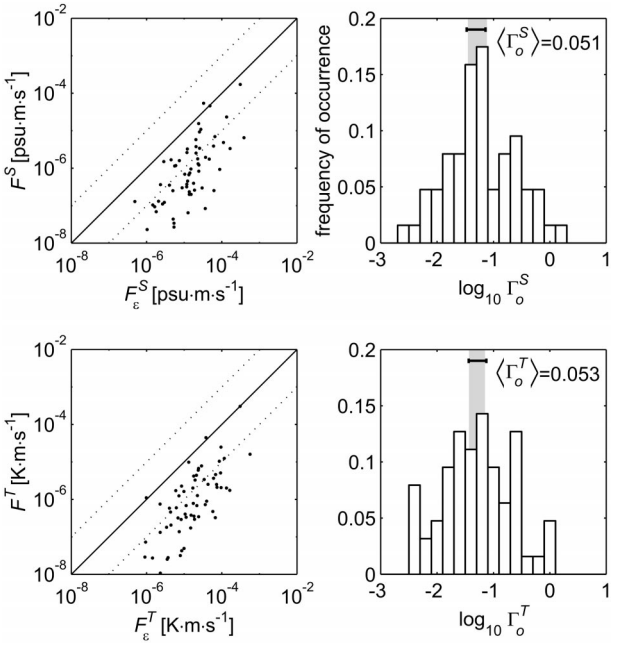

FIG. 13. Statistics of Γ_o, the flux coefficient based on the large-eddy transport. Data represents 76 patches with $|R_\rho| < 1$ and both $\langle w'T'\rangle$ and $\langle w'S'\rangle$ significant at the 95% level.

in Fig. 14. This indicates that the diffusivities of heat and salt based on eddy fluxes are, indeed, equal and $\langle d_o\rangle = 1$. However, the distribution of d_χ is shifted to smaller values, suggesting that salt may be less effectively diffused by turbulence than heat.

c. *Differential diffusion by turbulence?*

As a thought experiment to illustrate how differential diffusion might arise, consider the limiting case of mixing a scalar with infinitely small molecular diffusivity $D_\theta \to 0$, in a fluid parcel that evolves in time from quiescent to turbulent, and back to quiescent again. Assume that the scalar has some small effect on the buoyancy of the fluid. Scalar fluctuations produced by a turbulent overturn at large scales cascade to smaller scales as time evolves. After all turbulent motions subside, scalar gradients remain on a variety of scales but are not smeared by molecular diffusion. Given time, the scalar anomalies, each with a slight buoyancy anomaly, re-sort themselves and eventually return to the original scalar profile. The result? No irreversible mixing.

Now consider a real scalar with finite molecular diffusion in a viscous fluid. The scales at which gradients are smeared by molecular diffusion are characterized by the Batchelor wavenumber, $k_b^\theta \equiv [\epsilon/(\nu D_{\&thetas}^2)]^{1/4}$. We are primarily concerned with the cascade of variance to k_b^θ from the viscous wavenumber $k_\eta \equiv (\epsilon/\nu^3)^{1/4}$, a wavenumber band where the effect of molecular diffusivity becomes important (see Fig. 1: these are the viscous–convective and viscous–diffusive subranges of turbulence). Batchelor (1959) suggested that the transfer of variance in this subrange is dominated by the rate of least principal (most negative) strain $\gamma \sim -\sqrt{\epsilon/\nu}$, such that a Fourier wavenumber k (associated with some scalar gradient) evolves in time as $\sim ke^{-\gamma t}$. Scalar differ-

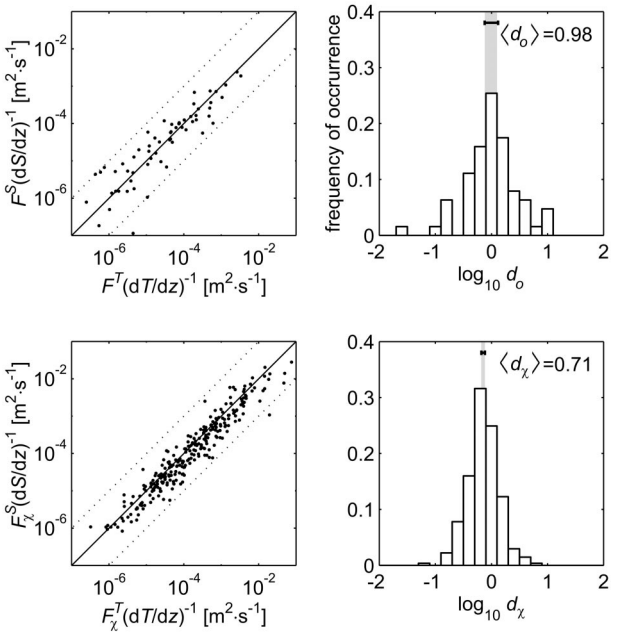

FIG. 14. Statistics of the diffusivity ratio based on large-eddy transports $d_o = (F_o^S/F_o^T)(dT/dS)$ (top) and based on the scalar dissipation rates $d_\chi = K_S/K_T$ (bottom).

ences over the Kolmogorov scale ($1/k_\eta$) are transformed into scalar differences over the much smaller Batchelor scale ($1/k_b^\theta$) by the compressive strain rate γ in time τ_θ, such that

$$k_b^\theta = k_\eta e^{-\gamma\tau_\theta}. \tag{17}$$

In this way, scalar gradients at small scales are increased.

For seawater (33 psu, 10°C, 0 dB) $\nu = 1.4 \times 10^{-6}$ m^2 s^{-1}, $D_T = 1.5 \times 10^{-7}$ m^2 s^{-1}, and $D_S = 1.0 \times 10^{-9}$ m^2 s^{-1} so that $k_b^S/k_b^T \sim 10$. The time it takes for a Fourier component to cascade from the Kolmogorov to the Batchelor wavenumber is

$$\tau_\theta = \frac{1}{|\gamma|} \ln \sqrt{\frac{\nu}{D_\theta}}. \tag{18}$$

For temperature fluctuations, $\tau_T = 1.1\sqrt{\nu/\epsilon}$, while for salinity, $\tau_S = 3.7\sqrt{\nu/\epsilon}$. Thus, it takes more than three times longer to cascade salinity variance into its diffusive scales than it does for temperature variance.

In the absence of persistent forcing,[4] the lifespan of a turbulent patch may be considered to be $\tau_{\text{patch}} \sim O(N^{-1})$ (Crawford 1986; Moum 1996b). If τ_{patch} is much shorter than the time it takes to cascade variance to the diffusive spatial scales, then there will be remnant salinity variance at moderately high wavenumbers ($k > k_b^T$) for which the corresponding temperature variance has already diffused away. If this salinity variance is able to re-sort itself through its buoyancy, we should expect incomplete mixing; consequently $P_\theta \neq \chi_\theta$.

Whether the remnant salinity variance is able to resort itself or remains in a statically unstable state to diffuse slowly through molecular diffusion depends on the Rayleigh number, Ra. Convective re-sorting of remaining salinity fluctuations ΔS should occur if Ra exceeds a critical value, $\text{Ra}_c \simeq 1000$ (Turner 1973). For our purposes

$$\text{Ra} = \frac{g\beta_o \Delta S l^3}{\nu D_S}, \tag{19}$$

where l is the length scale of the salinity fluctuations and $\beta_o \simeq 7.7 \times 10^{-4}$ psu^{-1} is the haline contraction coefficient. For salinity fluctuations typical of our data ($\Delta S = 0.01$ psu; see Fig. 4), convective re-sorting should occur for fluctuations with $l > 2.7$ mm. For a turbulent patch with $\epsilon = 10^{-9}$ m^2 s^{-3}, the length scale associated with the smallest temperature fluctuations ($l_T = 2\pi/k_b^T$) is 15 mm, whereas salinity variance extends to scales of $l_S = 2\pi/k_b^T = 1.2$ mm. It is therefore possible that salinity variance at large scales ($l > 2.7$ mm) will convectively re-sort, whereas fluctuations at small scales ($l < 2.7$ mm) will mix through molecular diffusion.

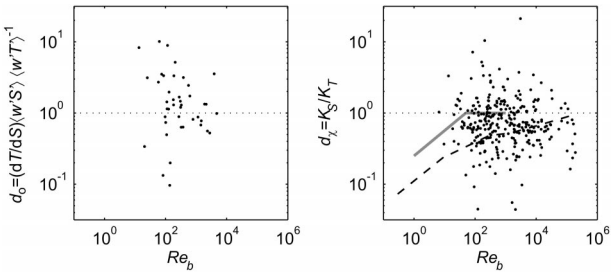

FIG. 15. Variation of the flux ratios d_o (based on the largeeddy transport) and d_χ (based on scalar dissipations) with buoyancy Reynolds number $\text{Re}_b \equiv \epsilon/(\nu N^2)$. For comparison, the dashed line represents the normalized salt to heat flux ratio (ϕ_S/ϕ_T) computed from Merryfield et al. (1998) for direct numerical simulation of two-dimensional turbulence. The solid line represents the ratio of saline to thermal entrainment velocity from the laboratory experiments of Turner (1968). We estimate Re_b for their experiments as discussed in the text.

We note that the ratio of time scales is proportional to the square root of the buoyancy Reynolds number $\text{Re}_b \equiv \epsilon/(\nu N^2)$ so that

$$\tau_{\text{patch}}/\tau_\theta = \beta_\theta \sqrt{\text{Re}_b}, \tag{20}$$

where $\beta_T \sim 0.9$ and $\beta_S \sim 0.3$. From the above discussion, we conclude that $K_S \simeq K_T$ for flows with large Re_b. For small Re_b, which describes weak and anisotropic turbulence, the arguments presented above suggest $K_S < K_T$.

The dependence of the flux ratios on Re_b is shown in Fig. 15. Because of the small dynamic range of Re_b and significant variability of our estimates, it is not possible to resolve a trend in our data. Also plotted for comparison is an estimated diffusivity ratio from Turner's (1968) laboratory experiments and the direct numerical simulations of Merryfield et al. (1998). Each curve exhibits a trend consistent with our intuitive arguments. Note that the DNS and lab experiments give quantitatively different ranges of Re_b where K_S/K_T is significantly less than one.

In Turner's experiments, turbulence was generated by an oscillating grid that eroded a temperature or salinity interface. The rate at which fluid mixed across the interface was described in terms of an entrainment velocity (u_e^T for temperature and u_e^S for salinity) and characterized with respect to a parameter resembling a Richardson number, but which depended on specific geometrical details of the experimental setup: $\text{Ri}_o = 3 \times 10^8 \Delta\rho/(\rho n^2)$, where $\Delta\rho/\rho$ is the fractional density step across the interface and n is the stirring rate in cycles per minute. Thompson and Turner (1975) later measured turbulent length and velocity scales (l, u) for a similar experimental setup, allowing Turner (1973) to relate the results to a more meaningful Ri.

To facilitate comparison with our oceanic data, we compute Re_b for Turner's experiments from unpublished

[4] For this analysis we consider the turbulent events to be freely decaying patches. Hence, our scaling is inappropriate if the duration of the forcing is much greater than N^{-1}, an example being the persistent mixing associated with near-inertial internal waves (Gregg et al. 1986).

data.[5] We estimate $\epsilon = u^3/l$ based on the turbulent velocity ($u = 8 \times 10^{-6} \times n$ m s^{-1}) and length scale ($l = 9$ mm) at the interface, using the measurements of Thompson and Turner (1975), $N^2 = g\Delta\rho/(\rho\Delta z)$ was computed using $\Delta z = 90$ mm (the mean separation between interface and grid) in order to represent the background stratification. Numerically, Re_b is approximately $\sim (90 - 270)\ \mathrm{Ri}^{-1}$, where Ri is that in Turner (1973). The flux ratio was computed as $d = u_e^S/u_e^T$. As shown in Fig. 15, Turner's experiments suggest that differential diffusion is appreciable only at low buoyancy Reynolds numbers ($\mathrm{Re}_b < 100$). We note, however, that the mixing of a two-layer fluid by grid turbulence is significantly different than that in ocean mixing, so that the direct comparisons like those in Fig. 15 should be interpreted cautiously.

Also plotted is the ratio of cumulative salt flux ϕ_S to heat flux ϕ_T as estimated from the numerical simulations of Merryfield et al. (1998). Although Re_b was not explicitly determined in their simulations, we estimate Re_b as Fr^2 Re (for runs I(a–c): red energy spectrum) and $12\mathrm{Fr}^2$ (for runs II(a–c): blue energy spectrum). These indicate that $0.5 < K_S/K_T < 0.9$ in the range $10^2 < \mathrm{Re}_b < 10^6$, which is consistent with our data.

d. Relationship between spectral shape and K_S/K_T

Figures 5 and 8 show that the spectral shapes Ψ_{T_z} and Ψ_{S_z} are similar to each other and that their dependence in the viscous–convective subrange is slightly less than the k^{+1} predicted by Corrsin (1951), Batchelor (1959), or Kraichnan (1968). A similar deviation from k^{+1} at low C_x (Dillon and Caldwell 1980; Oakey 1982; Gargett et al. 1984) has generally been associated with excess variance from background vertical microstructure. Since low C_x corresponds to low Re_b, we postulate that this elevated variance may also result from transfer of variance from the spectral peak to lower wavenumbers as a result of buoyant resorting. We argue that the spectral shapes of Ψ_{T_z} and Ψ_{S_z} described by universal forms with spectral slope in the viscous–convective subrange less than k^{+1}, as suggested by Fig. 11, are consistent with differential diffusion.

Assume that eddies stir T and S in a similar fashion so that the production of scalar variance, P_θ, is proportional to $(d\theta/dz)^2$. Spectral levels in the inertial subrange scale accordingly (with constant of proportionality C_θ: Sreenivasan 1996) so that

$$\Psi_\theta(k) = C_\theta P_\theta \epsilon^{-1/3} k^{1/3}, \tag{21}$$

an equation usually written in terms of χ_θ under the assumption that $P_\theta = \chi_\theta$.

We use geometrical arguments to determine the relationship between production and dissipation if the viscous–convective subrange scales as k^n instead of k^{+1} as predicted by Corrsin (1951) in Eq. (5). First, we assume the wavenumber extent of the gradient spectrum is proportional to k_b^θ. The amplitude of the peak of the viscous–diffusive subrange depends on the spectral level at the Kolmogorov wavenumber (the source of variance for the viscous–convective cascade), which scales with $(d\theta/dz)^2$. It also depends on the bandwidth and spectral slope of the viscous–convective subrange and is, thus, also proportional to $(k_b^\theta)^n$. Hence, $\Psi_{\theta_z}^{\max} \propto (d\theta/dz)^2\,(k_b^\theta)^n$.

The dissipation rate is the integral of the scalar gradient spectrum, which is proportional to the product of the bandwidth and amplitude of the spectral peak:

$$\chi_\theta = 6D_\theta \int_0^\infty \Psi_{\theta_z}(k)\, dk \propto D_\theta \Psi_{\theta_z}^{\max} k_b^\theta \propto D_\theta (k_b^\theta)^{n+1} (d\theta/dz)^2. \tag{22}$$

We can now evaluate K_S/K_T using Eqs. (3) and (22):

$$\frac{K_S}{K_T} = \frac{D_S (k_b^S)^{n+1}}{D_T (k_b^T)^{n+1}} = \left(\frac{D_S}{D_T}\right)^{(1-n)/2}. \tag{23}$$

Evaluating Eq. (23) we find $K_S/K_T = 0.7$ for a spectral slope of $n = 0.85$; integration of the Kraichnan spectrum (modified to have a $k^{0.85}$ viscous–convective subrange as plotted in Fig. 16) yields the same result. Hence, the equivalence of K_S and K_T relies on the spectral slope in the viscous–convective subrange to be $+1$, as long as the extent of the spectrum scales with k_b^θ. Our finding that d_χ is less than one (Fig. 14) is therefore consistent with Ψ_{T_z} and Ψ_{S_z} having similar shape and an $\sim k^{+0.85}$ viscous–convective subrange.

Figure 16 shows the observed gradient spectra in relation to the Kraichnan universal spectrum, both in its original form and that with a $k^{+0.85}$ viscous–convective subrange. We sort the data by buoyancy Reynolds number: the spectra in Fig. 16a are calculated from patches with $\mathrm{Re}_b > 1000$ and may be expected to be quasi-isotropic; the spectra in Fig. 16b are calculated from patches with low Re_b where the influence of buoyancy may be significant. Clear differences in the spectra are observed at low wavenumber. For $\mathrm{Re}_b > 1000$, spectral levels of Ψ_{T_z} and Ψ_{S_z} converge for $\alpha^\eta < 1$. In contrast, for patches with $\mathrm{Re}_b < 1000$, normalized spectral levels exceed those of the universal spectrum at low wavenumbers, consistent with the observations of temperature microstructure at low C_x by Dillon and Caldwell (1980) and others.

As a result, normalized spectra of S exceed those of T in the viscous–convective subrange at low Re_b (Fig. 16b). Since the spectra have been normalized by χ_T and χ_S, the differences in spectral amplitudes at low wavenumbers represent the relative excess of production over dissipation, assuming that spectral levels at low wavenumbers are associated with P_θ. As a consequence, there is a different relationship between production (P_θ, given by the spectral level at low k), and dissipation

[5] We thank Stewart Turner for locating his 35 year old Cambridge laboratory notebook and kindly providing this data to us.

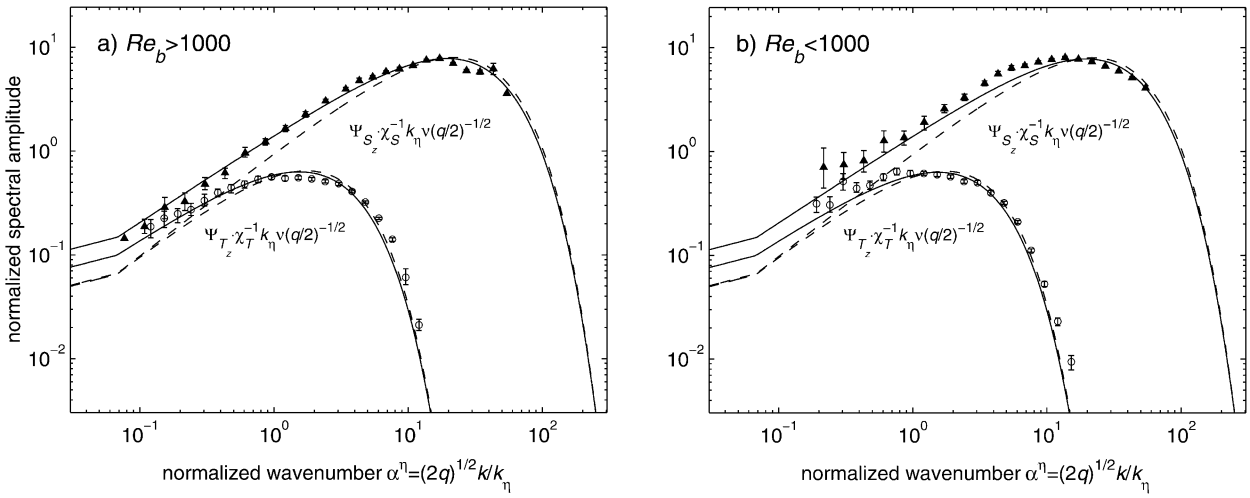

FIG. 16. Gradient spectra calculated from patches with (a) high Re_b and (b) low Re_b exhibit subtle but important differences in spectral shape, especially at low α^η. More than 150 patches contribute to each range of Re_b; normalization and symbols are the same as in Fig. 11a; error bars represent 95% bootstrap confidence limits. The dashed curves represent Kraichnan's universal scalar gradient spectrum; the solid lines represent a modified Kraichnan spectrum in which the viscous–convective subrange scales with $k^{+0.85}$ instead of k^{+1}. An approximate agreement between observations and the modified universal spectrum (particularly for low-Re_b) suggests that the spectral slope in the viscous–convective subrange may be less than 1.

(χ_θ, the integral of Ψ_{θ_z} used to normalize the data) for S as compared to T. We may express this as

$$P_\theta = \chi_\theta + \text{undissipated}, \tag{24}$$

where the amount not dissipated is related to the elevation of spectral levels above a k^{+1} viscous–convective subrange and is greater for S than for T at low Re_b. This Re_b dependence is consistent with our arguments in the previous section.

We emphasize that we are unable to give a theoretical or analytical justification for our choice of spectral slope at this time: we simply suggest that a $k^{+0.85}$ viscous–convective subrange is not inconsistent with our observed spectra (particularly at low Re_b) and that such a slope followed by a diffusive cutoff $\propto k_b^\theta$ is consistent with $K_S/K_T = 0.7$ and the possibility of differential diffusion.

5. Conclusions

Highly resolved measurements of salinity have been made from a vertical microstructure profiler near the coast of Oregon. Four hundred patches of turbulence were analyzed from which the spectrum of salinity gradient Ψ_{S_z} was determined. The spectrum of salinity gradient exhibits an approximate k^{+1} behavior in the viscous–convective subrange, followed by a diffusive rolloff that closely resembles the universal form of Kraichnan (1968). From Ψ_{S_z}, the dissipation rate of salinity variance χ_S was calculated and the eddy flux $\langle w'S'\rangle$ was estimated. Such quantities permit the turbulent transport of salinity to be estimated and compared to that for temperature.

We use d_o, the ratio of the transport of T and S on eddy scales, to compare the covariance fluxes of heat and salt, $\langle w'T'\rangle$ and $\langle w'S'\rangle$. Our finding that $\langle d_o\rangle \sim 1$ suggests that T and S are transported equally well by the large-scale eddy field. This contrasts our estimate of $\langle d_\chi\rangle = \langle K_S/K_T\rangle$, which describes the observed flux due to irreversible mixing and represents the ratio of eddy diffusivities. The distribution of d_χ exhibits much scatter (~two decades), and has a geometric mean $\langle d_\chi\rangle = 0.7$ (Figs. 14 and 15). We present this value along with the following words of caution. As discussed in the appendix, there are several sources of error that may bias our estimates: we estimate that $0.6 < \langle d_\chi\rangle < 1.1$ are probable bounds on our estimates of K_S/K_T. This error arises primarily from 1) our thermistor response corrections, 2) the assumption of isotropy in estimating χ_S and χ_T from one-dimensional vertical gradient spectra, and 3) our use of the Kraichnan universal spectrum (and the value of q), to correct for unresolved variance during spectral integration. In addition, these measurements represent a limited number of turbulent patches in a small subset of the oceanic parameter space; one important restriction within our analysis was the requirement that $|R_\rho| < 1$. Furthermore, we have biased our data by selecting only turbulent patches for the analysis and neglecting weakly turbulent ones (for which differential diffusion is more probable). While our results are highly suggestive that $d_\chi < 1$, our estimated uncertainty does not rule out the possibility that $d_\chi = 1$, and from this limited dataset, we are unable to make a general claim for the value of K_S/K_T in the global ocean, or for its dependence on Re_b.

Although the eddy motions produce variance of T and S proportional to $(dT/dS)^2$, a value of $d_\chi < 1$ would suggest that all of this variance is not dissipated. In

particular, a disproportionate amount of the salinity variance is not being dissipated because of its low molecular diffusivity. It would be assumed that this variance eventually restratifies because the duration of the turbulent patch is not sufficient to allow complete irreversible mixing by molecular processes. This can only happen at low Re_b and sufficiently high Ra, both of which imply weak, anisotropic turbulence. The observed spectral slope in the viscous–convective subrange for low Re_b patches is consistent with an imbalance of production over dissipation.

While these are the first estimates of the irreversible salinity flux in the ocean, evidence that the irreversible transport for salt is less efficient than that for heat is not new. Our estimates of d_χ are consistent with those from the numerical experiments of Merryfield et al. (1998), who found the normalized flux ratio of salt to heat to be significantly less than one over a similar range of Re_b, as shown in Fig. 15. The experiments of Turner (1968) suggest that differential diffusion ($d_\chi < 1$) should be significant only at much smaller buoyancy Reynolds numbers ($\mathrm{Re}_b < 100$). The discrepancies between each of these experiments needs further investigation.

6. Potential consequences

The possibility that heat and salt are transported through the ocean at different rates has significant consequences. Most importantly, vast regions of the ocean are characterized by small buoyancy Reynolds number (Re_b), where incomplete mixing is possible. Gargett and Holloway (1992) and others have suggested that small differences in the eddy diffusivities of heat and salt could have a significant impact on the thermohaline circulation.

Secondly, oceanographers have relied on the eddy diffusivity of heat—the quantity that the microstructure community usually measures—as being representative of that of salt, density, and buoyancy. While in regions of energetic turbulence this should be the case, in regions where salinity plays a dominant role in determining the stratification and where turbulence is weak it is likely that K_ρ may be less than expected.

Finally, these results might further the interpretation of tracer-release experiments (Ledwell et al. 1993). The tracers used in those experiments generally have a molecular diffusivity comparable to that of salt,[6] so that the inferred diffusivity is more closely related to K_S than to K_T or K_ρ. It is therefore possible that these experiments tend to underestimate the true irreversible mixing of temperature or density, if indeed the turbulent diffusivities of heat and salt are unequal. This is especially likely in the regions of low turbulence levels where the dye release experiments have been relied upon to deliver bulk estimates of eddy diffusion coefficients. A quantitative understanding of the dependence of K_S/K_T on Re_b will help to refine error estimates on diffusivities derived from such experiments.

These results highlight the need to develop a theoretical framework to relate the probability of incomplete mixing to flow parameters like the buoyancy Reynolds number. It should be possible to perform laboratory and numerical experiments to clarify some of the issues raised here and gain a more precise and fundamental understanding of d_χ. Future experiments should be designed to improve our understanding of the aspects that contribute to most of the uncertainty in the estimate of d_χ, namely the role of anisotropy in differential diffusion (and our ability to measure it) and the shape of the diffusive subrange of scalar gradient variance at a variety of Re_b. More extensive measurements of both horizontal and vertical scalar gradient in the low-Re_b regime will be needed to clearly determine the variability (or lack thereof) of K_S/K_T.

Acknowledgments. The authors have benefitted from informative discussions with Bill Smyth, Roland de Szoeke, Doug Caldwell, Jen MacKinnon, and Eric Kunze. The technical support of Michael Zelman, Mike Neeley-Brown, Ray Kreth, Gunnar Gunderson, and Greig Thompson made these measurements possible. We thank Stewart Turner for providing us with data from his 1966 experiments. This manuscript has benefitted from the critical and insightful comments of an anonymous reviewer. Funding by the Office of Naval Research and the National Science Foundation made this work possible.

APPENDIX

Sources of Error and Bias

To understand the limits and significance of the Osborn–Cox estimate of diffusivity and associated fluxes, quantification of the error and/or bias introduced into the spectra (Ψ_{S_z} and Ψ_{T_z}), the dissipations (χ_S and χ_T), and the mean gradients (dS/dz and dT/dz) is necessary.

Six significant sources of error that influence the preceding calculations are investigated and are summarized below.

(a) Signal attenuation: A careful description of the frequency response of the microbead thermistor has been determined by in situ comparisons with benchmark sensors. A theoretical and laboratory-verified spatial correction was applied to the conductivity probe. Such corrections to the power response can be determined to within a ±10% accuracy; since these corrections represent an average of 40% of the measured variance, the effect on the total measured variance is <10%.

[6] The molecular diffusivity of SF_6, used by Ledwell et al. (1993), is $D_{SF_6} = 8 \times 10^{-10}$ m^2 s^{-1} at 10°C (King and Saltzman 1995).

(b) Sensor noise: To calculate χ_θ, gradient spectra have been integrated over a wavenumber range limited by $k^\theta_{\max}$, the wavenumber where spectral amplitudes intersect an empirical noise spectrum. As a result, some noise may be included in high-k spectral estimates, causing the highest wavenumbers to be biased slightly high. Since spectral levels near the high wavenumbers are small, the effect of this noise on the total gradient variance (χ_S or χ_T) is small (0.6%).

(c) Estimation of dS/dz and dT/dz: There are several ways that the mean gradients can be calculated; the average error is 3%.

(d) Cospectrum $\Psi_{C_zT_z}$: A lag between T and C results in aliasing variance from the cospectrum into the imaginary part of the cross spectrum. Such phase errors may have biased χ_S low by 2%.

(e) Effect of anisotropy on χ_θ estimates from vertical spectra: Vertical gradient scalar spectra are enhanced over horizontal spectra at low Re_b. Because motions become more isotropic at higher wavenumbers, the variance of salinity gradient is more isotropic than that of temperature gradient, which occurs at larger scales. As a result, estimates of χ_T may be biased high whereas estimates of χ_S are likely to be unbiased (or at least less biased). Estimates of χ_S/χ_T may be significantly biased low at very low Re_b. Using an empirical relation derived from the direct numerical simulations of Smyth and Moum (2000), we find that χ_S/χ_T may be biased 10% low on average; however, the bias is less than 2% for $\mathrm{Re}_b > 200$.

(f) Choice of the form of the universal spectrum (Kraichnan or Batchelor), and the value of the constant q: This parameter relates the least principal strain rate to the dissipation rate ($\gamma = -q^{-1}\sqrt{\epsilon/\nu}$) and alters the wavenumber extent of the universal form for a given k_b. The error that can be introduced into the ratio χ_S/χ_T by assuming an improper spectral shape for integration correction can exceed 20%. Any bias in our estimate of $k_b \propto \epsilon^{1/4}$ is implicitly considered (as a bias in q).

Given the magnitude of these individual sources of error, we can place error bounds on our estimate of $d_\chi = K_S/K_T$. Thermistor attenuation, sensor noise, and error in estimation of mean gradients are random and add to produce an error of $\pm 14\%$. Phase errors and the effect of anisotropy may have biased d_χ low by as much as -12%. The shape of the universal spectrum (and the value of q) used for integration correction has significant effect on d_χ; for plausible values of q, $0.68 < d_\chi < 0.84$. Combining each of these errors gives a maximum range for $d_\chi = K_S/K_T$ of $0.57 < d_\chi < 1.06$. For the purpose of discussion in this paper, we round this to $0.6 < d_\chi < 1.1$. From this error analysis, it is suggestive that $d_\chi < 1$; at the same time, however, it is impossible to distinguish d_χ from unity, and thus $K_S = K_T$ is possible.

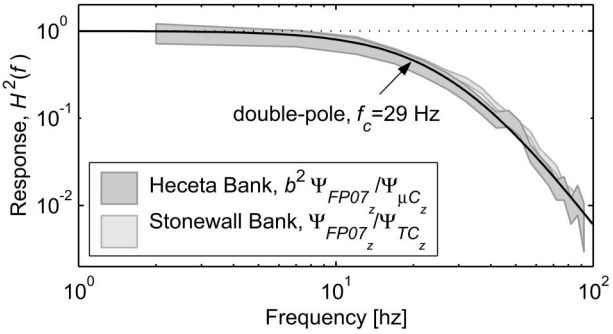

FIG. A1. The frequency response [$H^2(f)$] of the FP07 thermistors. Each shaded region represents the 95% bootstrap confidence interval for the average over at least 10 patches. The dark shading represents the response of the thermistor used at Heceta Bank, calculated as $H^2 = b^2\Psi_{\mathrm{FP07}_z}/\Psi_{\mu C_z}$, and the light shading represents that from the Stonewall Bank experiment, calculated as $H^2 = \Psi_{\mathrm{FP07}_z}/\Psi_{TC_z}$. A double-pole filter with f_c is shown as the smooth curve.

a. Probe response

1) TEMPERATURE

In this analysis, we consider Ψ_{T_z} at high wavenumbers ($k > 100$ cpm) where the FP07 response is highly attenuated. If the power-response transfer function,

$$H^2 = \frac{(\Psi_{T_z})_{\mathrm{measured}}}{(\Psi_{T_z})_{\mathrm{actual}}}, \tag{A1}$$

can be identified, then we can correct for variance not resolved directly by the thermistor. We estimate $(\Psi_{T_z})_{\mathrm{actual}}$ in situ using a fully resolving benchmark: either our ultrafast thermocouple probe or the μC probe in regions where the conductivity fluctuations are dominated by temperature. We define the temperature gradient spectrum measured by the FP07 thermistor, thermocouple probe, and μC sensor as Ψ_{FP07_z}, Ψ_{TC_z}, and $\Psi_{\mu C_z}$ respectively.

During the Heceta Bank experiment, there were many turbulent patches where the conductivity was dominated by temperature, and $\Psi_{\mu C_z}/b^2$ is representative of $(\Psi_{T_z})_{\mathrm{actual}}$ at wavenumbers below k_b^T. An ensemble average of the relative spectral amplitude, $b^2\Psi_{T_z}/\Psi_{\mu C_z}$ was calculated for 20 patches having $dT/dS > 20$ K/psu to determine the transfer function of the thermistor, and is plotted in Fig. A1. For these patches, the contribution of Ψ_{S_z} to Ψ_{C_z} was less than 0.1% for any given spectral estimate.

No turbulent patches with $dT/dS > 20$ K/psu were observed at Stonewall Bank, making it difficult to use the μC sensor to determine the thermistor time constant. Instead, the thermocouple was used as a benchmark, which we believe to respond without attenuation at 100 Hz (Nash et al. 1999).

For both experiments, the attenuation by the FP07 thermistor is well represented as a double-pole filter (Gregg and Meagher 1980) with $f_c = 29$ Hz:

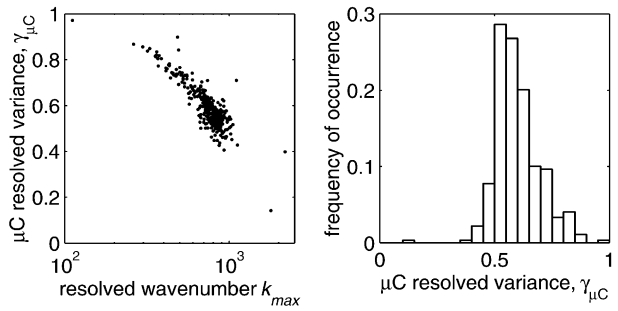

FIG. A2. Relationship between resolved wavenumber and the fraction of variance resolved by the fast conductivity probe $\gamma_{\mu C}$ (left). A histogram of $\gamma_{\mu C}$ is shown to the right; an average of 60% of the variance is resolved.

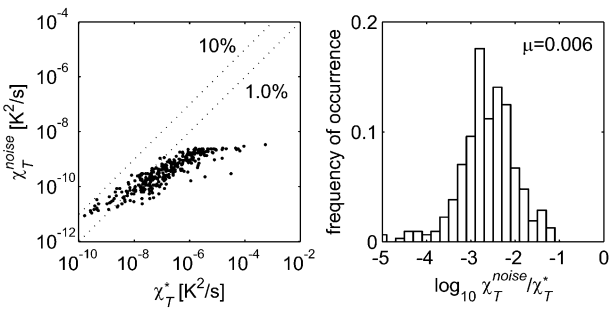

FIG. A3. Contribution of thermistor noise to estimates of χ_T. Dotted lines in the scatterplot (left) indicate cases where noise represents 1% and 10% of the measured temperature variance. On average, noise represents 0.6% of the signal (histogram, right). χ_T^{noise} is less than 2% of χ_T^* in 96% of the patches.

$$H^2(f) = \left(\frac{1}{1 + (f/f_c)^2}\right)^2. \tag{A2}$$

The 95% bootstrap limits on the mean fall within 10% of this form, providing confidence that correction of temperature spectra using $\Psi_{T_z}(f) = \Psi_{\mathrm{FP07}_z}(f)/H^2(f)$ will restore the true variance to within 10%.

2) CONDUCTIVITY

The response of the fast conductivity probe is described in Head (1983) and Nash and Moum (1999). Its spatial resolution is limited by the spatial extent of the induced conductivity field and has a wavenumber response similar to that of a single-pole filter,

$$H^2(k) = \frac{1}{1 + (k/k_c)^2}, \tag{A3}$$

where $k_c = 455$ cpm is the critical wavenumber. Using this form, half of the variance is attenuated by the μC sensor in a spectrum which extends to 1000 cpm. We define the fraction of conductivity variance resolved as

$$\gamma_{\mu C} = \frac{\int_0^{k_{\max}} H^2(k)\Psi_{C_z}(k)\, dk}{\int_0^{k_{\max}} \Psi_{C_z}(k)\, dk}, \tag{A4}$$

where Ψ_{C_z} represents resolved spectral amplitudes. For the patches analyzed, the mean fraction of variance resolved by the probe is 60%; its distribution is shown in Fig. A2. Assuming that we have properly described $H^2(k)$ to within 10%–20%, the error introduced into the variance of spectral estimates is at most 10%.

b. Error from sensor noise

To avoid contamination of χ_T by sensor noise, gradient spectra are integrated over the subrange $0 < k < k_{\max}^T$ [Eq. (10)], where $k_{\max}^T$ represents the wavenumber where spectral levels intersect the noise continuum. Thermistor noise within this interval will nevertheless contribute to χ_T. To determine this contribution, the thermistor noise spectrum (see Fig. 8 in Nash et al. 1999) is integrated over $0 < k < k_{\max}^T$ to estimate χ_T^{noise}, and compared to χ_T^*, the total temperature gradient variance integrated over the same wavenumber band (both integrals are multiplied by $6D_T$ to give dissipation units of $\mathrm{K}^2\ \mathrm{s}^{-1}$.). The relationship between χ_T^{noise} and χ_T^* is shown in Fig. A3.

In 96% of the patches, the contribution of sensor noise to the temperature gradient variance is less than 2%. Only in four of the weakly turbulent patches, where $\chi_T < 5 \times 10^{-10}\ \mathrm{K}^2\ \mathrm{s}^{-1}$ does χ_T^{noise} exceed 5% of χ_T^*; noise never exceeds 10% of the signal. On average, thermistor noise represents 0.6% of χ_T^* and is therefore unlikely to appreciably bias χ_T or the ratio of χ_S/χ_T. Noise in the conductivity sensor has a similar small effect on our estimates of χ_S.

c. Error in dT/dz, dS/dz

Estimates of K_θ are sensitive to error introduced in the determination of the background vertical scalar gradient $d\theta/dz$. For example, the comparison of K_S/K_T is sensitive to error or bias in the ratio $[(dT/dz)/(dS/dz)]^2$.

To investigate the magnitude of this error, the minimum and maximum of each estimate of dT/dz and dS/dz was calculated using a linear regression at the 95% confidence level. Each patch was resorted in two ways: with respect to density and with respect to each scalar. Defining the fractional error as $\Delta_{dT/dS}$,

$$\Delta_{dT/dS} = \left(\frac{(dT/dz)_{\max}}{(dS/dz)_{\min}}\right)\left(\frac{(dT/dz)_{\min}}{(dS/dz)_{\max}}\right)^{-1} - 1, \tag{A5}$$

where min(max) refer to the minimum(maximum) using either method to determine the gradient. The distribution of the fractional error is shown in Fig. A4. The average error is 3% for the patches used in this analysis, having $\Delta_{dT/dS} < 0.2$.

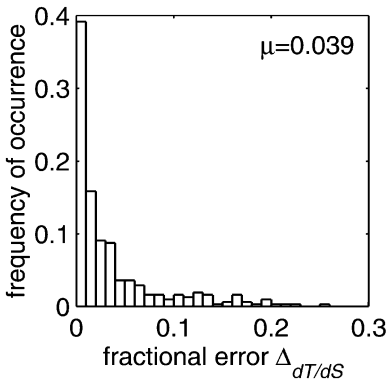

FIG. A4. Distribution of fractional error $\Delta_{dT/dS}$ in dT/dS which results from estimating the mean background gradient of dT/dz and dS/dz using a linear regression with 95% confidence and two methods of resorting.

d. Errors specific to χ_S: The T–C phase

Since Ψ_{S_z} depends on the real part of the complex *T–C* cross-spectrum, the relative phase between the μC sensor and FP07 thermistor signals must be determined. Otherwise, the real component of the cross spectrum is aliased into the imaginary component and tends to reduce the magnitude of the cospectrum $\Psi_{C_zT_z}$. The phase lag between *T* and *C* depends on 1) the phase response associated with the μC sensing volume, 2) the thermal transfer rate across the FP07's boundary layer and glass insulation, and 3) the spatial separation between the microbead FP07 thermistor and the μC sensing volume.

While the phase lag $\phi_{\mu C}$ associated with the μC sensor is likely small (but remains to be quantified) over the low wavenumbers where $\Psi_{C_zT_z}$ is significant, the inherent phase lag of the FP07 and the lag resulting from the spatial separation between sensors are not negligible. The phase lag of a thermistor with double-pole response (Gregg and Meagher 1980) is $\phi_{\text{FP07}} = 2\tan^{-1}(f/f_c)$, with $f_c = 29$ Hz, which can be linearized ($\phi_{\text{FP07}} = 2f/f_c$) for small f/f_c. The phase associated with the spatial separation *d*, is $\phi_{\text{sep}} = 2\pi f(d/W_o)$, where $d \sim$ 2–4 mm, depending on the μCT probe.

Because the μC phase response and the spatial separation between sensing volumes are not easily measured, we determined $\phi_{\text{lag}} = \phi_{\mu C} + \phi_{\text{FP07}} + \phi_{\text{sep}}$ empirically by assuming the linearized form of τ_{FP07} such that $\phi_{\text{lag}} \simeq 2\pi f\tau_{\text{lag}}$. In the time domain, τ_{lag} simply represents a time lag between sensors and was chosen to produce zero phase difference between *T* and μC for the ''average'' temperature-dominated patch. For our μCT sensors, $\tau_{\text{lag}} = 14$–18 ms.

Some deviation in the *T–C* phase from the expected 0° or 180° was observed from patch to patch.[A1] To investigate the role that an improper phase lag would play on the estimation of χ_S, an analysis was performed that restricted the phase between *C* and *T* to either 0° or 180°. It was found that the mean difference between χ_S calculated in this manner and χ_S calculated from the observed phase was less than 2%. This small error can be rationalized by realizing that the cospectrum is sensitive to the cosine of the phase, so a 10° mismatch in phase (near $\phi = 0°$ or $\phi = 180°$) only lowers the spectrum by 1.5%.

e. Bias associated with anisotropy

The ratio of the length scale where buoyancy effects are important [the Ozmidov scale: $L_o = (\epsilon/N^3)^{1/2}$] to the length scale where viscous effects are important [the Kolmogorov scale: $L_k = (\nu^3/\epsilon)^{1/4}$] is $L_o/L_k = \text{Re}_b^{3/4}$. As Re_b becomes small, dissipation scales become increasingly influenced by buoyancy, the inertial subrange collapses, and velocities in the viscous subrange become anisotropic (Gargett et al. 1984). At yet lower Re_b, the diffusive subrange becomes anisotropic as well (Itsweire et al. 1993; Smyth and Moum 2000). In this section, we estimate the possible effect of anisotropy on estimates of χ_S/χ_T (or equivalently K_S/K_T).

Vertical gradients are enhanced over horizontal gradients at scales $O(L_o)$. At low -Re_b, estimates of χ_θ based on Ψ_{θ_z} alone (which we denote as χ_θ^z) will therefore be biased high by at most a factor of 3 if isotropic relations $\langle(d\theta/dx)^2\rangle = \langle(d\theta/dy)^2\rangle = \langle(d\theta/dz)^2\rangle$ are assumed (Smyth and Moum 2000). Because the diffusive scales for *S* are smaller than those for *T*, at a given Re_b the dissipation subrange of *S* is more isotropic than that of *T*. Smyth and Moum (2000) report that the degree of anisotropy scales with C_x and becomes important for $C_x < 100$. Since the Cox number for *S* is $\sim$100$\times$ that for *T* [$C_x^S \sim (D_T/D_S)C_x^T$] and each Cox number scales approximately with Re_b, ($C_x^T \sim 0.35\text{Re}_b$ in our data, $C_x^S \sim 35\text{Re}_b$), we should expect $\chi_T < \chi_T^z$ for $\text{Re}_b < 300$ but $\chi_S \simeq \chi_S^z$ for $3 < \text{Re}_b < 300$.

Because we have no way to directly measure the anisotropy of our turbulent patches, we quantify the effect of anisotropy using the direct numerical simulations of Smyth and Moum (2000, their Fig. 20c), which give a qualitatively similar relationship to that of Itsweire et al. (1993). Defining $m^\theta = \chi_\theta^z/\chi_\theta$ as the ratio of χ_θ^z based on vertical gradients to the real χ_θ, a very approximate empirical relation for the isotropy ratio is $m^\theta = 1$ for $C_x > 100$, $m^\theta = 3$ for $C_x < 1$, and $\log m^\theta = (\log 3)(1 - 0.5\log C_x^\theta)$ for $1 < C_x < 100$ (Fig. A5). Applying this relation to our data, the fraction that χ_S/χ_T is underestimated based on vertical gradient spectra and the assumption of isotropy is $m_S/m_T = (\chi_S^z/\chi_T^z)/(\chi_S/\chi_T)$ and is plotted in Fig. A6 for our turbulent patches.

Figure A6 indicates that χ_S^z/χ_T^z may underestimate χ_S/χ_T by at most a a factor of 3 at the lowest Re_b. Most estimates ($\sim$70%) are at high Re_b and are unaffected by anisotropy. The remaining 30% of the patches are affected to varying extents, and the average effect is to

[A1] The expected values of *T–C* phase over wavenumbers where molecular processes are insignificant is either 0° or 180°, depending on the *T–S* relation.

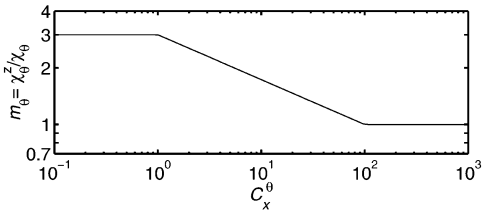

FIG. A5. Approximate empirical description for the anisotropy ratio, m_θ, derived from Fig. 20c of Smyth and Moum (2000).

bias our estimate of χ_S/χ_T low by 10%. For $\mathrm{Re}_b > 200$, the ratio χ_S/χ_T is biased low by less than 2% on average. At lower buoyancy Reynolds numbers, the bias is possibly significant, complicating the interpretation of trends in Figs. 14 and 15.

This Prandtl number dependent bias in estimating χ highlights the difficulty of understanding the Re_b dependence of $d_\chi = K_S/K_T$. This is because the Re_b range where one might expect $d_\chi < 1$ is precisely the same range where anisotropy affects our estimates of χ_T and χ_S. While the anisotropy of the flow at low Re_b is a possible mechanism for generating unequal eddy diffusivities of heat and salt, at the same time it complicates our ability to measure those diffusivities. A more complete description of how anisotropy affects the diffusive scales in weakly turbulent, multicomponent flows seems necessary if we are to understand how K_S/K_T varies under a variety of Re_b. Obtaining horizontal spectra may play a key role in this problem.

f. Error estimating χ_θ

The use of a universal scalar spectrum represents the largest source of error in estimating χ_θ from under-resolved spectra. The assumption of either the Kraichnan or Batchelor universal forms and the value of the parameter q affects the amount of variance assumed to be outside our limits of integration when determining χ from Ψ. Figure A7 shows the distribution of q as determined by comparing Ψ_{T_z} with ϵ, following the method of Luketina and Imberger (2001).

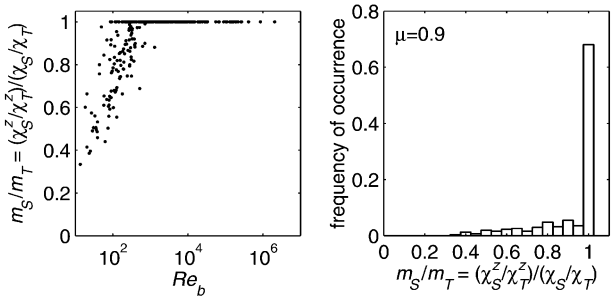

FIG. A6. Estimated effect of anisotropy on the scalar dissipation ratio from vertical gradients alone, based on the empirical relation in Fig. A5. m_S/m_T represents the fractional amount χ_S^z/χ_T^z underestimates the true χ_S/χ_T. Most patches (~70%) are isotropic; and if only $\mathrm{Re}_b > 200$ are considered, the average effect is to bias d_χ by 2%. However, at very low Re_b, where effects of differential diffusion are possible, anisotropy dramatically affects estimates of d_χ and m_S/m_T can approach 1/3.

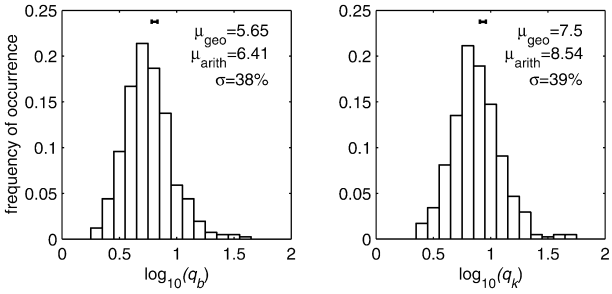

FIG. A7. Distribution of q_b (left) and q_k (right) from the comparison of Ψ_{T_z} with ϵ, following the method of Luketina and Imberger (2000). The 95% bootstrap confidence limits on the means are $6.0 < q_b < 6.8$ and $8.0 < q_k < 9.1$.

While the bootstrap confidence limits on the mean are relatively small, the distribution of estimates spans a factor of 2. Only 50% of the estimates fall in the range $4.2 < q_b < 7.5$ and $5.5 < q_k < 10.3$. We use these as ranges to test the effect of the value of q on our estimates of χ_T and χ_S by using a universal spectral form for integration correction.

The effect of the value of q and the choice of the

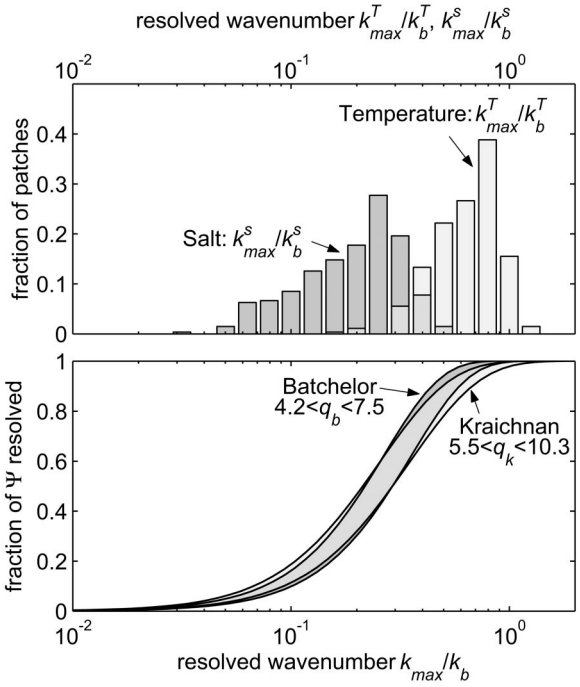

FIG. A8. Fraction of the salinity and temperature gradient variance resolved. The upper plot shows the distribution of the resolved wavenumber for salinity $k_{\max}^s/k_b^S$ (dark shading) and that for temperature $k_{\max}^T/k_b^T$ (light shading). The fraction of variance measured ($6D_\theta \int_0^{k_{\max}^\theta} \Psi_\theta \, dk/\chi_\theta$) depends on the theoretical form (Kraichnan or Batchelor) and the value of q, as indicated in the lower figure. For temperature, 99% of the spectra contain at least 50% of the variance; for salinity, only 27% of the spectra resolve more than 50% of the variance.

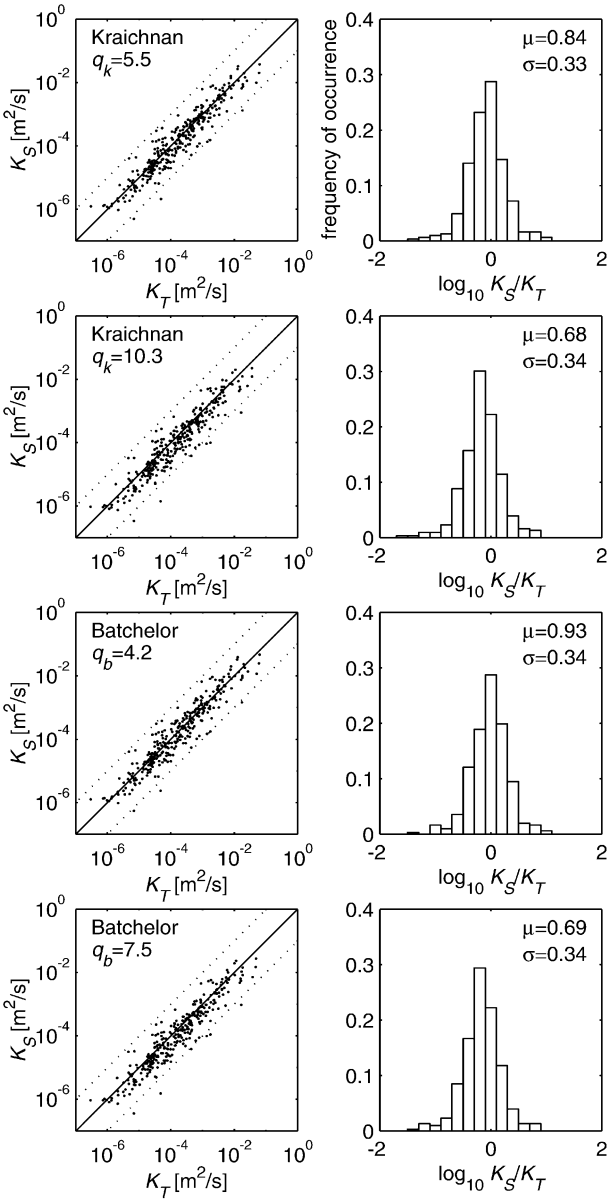

FIG. A9. Effect of the form of the universal scalar spectrum (used for integration correction), on the ratio of K_S/K_T.

universal spectral form (Kraichnan or Batchelor) on the fraction of variance resolved by our measurements (i.e., the correction factor which needs to be applied to unresolved spectra) is shown in Fig. A8. The degree to which this affects the estimate of K_S/K_T can be significant; compared to estimates made using the Kraichnan form and $q_k = 7.5$, a bias of 15% in d_χ could be introduced by choosing the incorrect universal form (Fig. A9). Note that the choice of q has less effect on K_S/K_T when the Kraichnan spectrum is used; this is likely the result of the Kraichnan spectrum more closely matching the observations. Since the value $q_k = 7.5$ was chosen for this analysis because it best matches the spectral shape of scalar gradients, it would be surprising if the extreme values presented in Fig. A8 described the real spectra of our observations.

We also note that observed spectral levels of T and S in the viscous–convective subrange exceed those of theoretical forms (Fig. 11b). As a result, the use of Eq. (10) to correct for lost variance will overestimate χ_θ for poorly resolved spectra. Since T is generally better resolved than S (Fig. A8), χ_S/χ_T may be biased slightly high from this effect. However, the similarity of the nondimensionalized spectra of Ψ_{S_z} and Ψ_{T_z} (Fig. 11b) and the fact that we observe $d_\chi < 1$ would both suggest that this bias is not large.

REFERENCES

Altman, D. B., and A. E. Gargett, 1990: Differential property transport due to incomplete mixing in a stratified fluid. *Stratified Flows*, E. List and G. Jirka, Eds., American Society of Civil Engineers, 454–460.

Batchelor, G. K., 1959: Small-scale variation of convected quantities like temperature in turbulent fluid. *J. Fluid Mech.*, **5,** 113–133.

Bogucki, D., J. Domaradzki, and P. Yeung, 1997: Direct numerical simulations of passive scalars with $Pr > 1$ advected by turbulent flow. *J. Fluid Mech.*, **343,** 111–130.

Corrsin, S., 1951: On the spectrum of isotropic temperature fluctuations in isotropic turbulence. *J. Appl. Phys.*, **22,** 469–473.

Crawford, W. R., 1986: A comparison of length scales and decay times of turbulence in stably stratified flows. *J. Phys. Oceanogr.*, **16,** 1847–1854.

Dillon, T. M., and D. R. Caldwell, 1980: The Batchelor spectrum and dissipation in the upper ocean. *J. Geophys. Res.*, **85** (C4), 1910–1916.

Gargett, A. E., 2002: Differential diffusion: An oceanographic primer. *Progress in Oceanography*, Pergamon, in press.

——, and G. Holloway, 1992: Sensitivity of the GFDL ocean model to different diffusivities of heat and salt. *J. Phys. Oceanogr.*, **22,** 1158–1177.

——, and J. N. Moum, 1995: Mixing efficiencies in turbulent tidal fronts: Results from direct and indirect measurements of density flux. *J. Phys. Oceanogr.*, **25,** 2583–2608.

——, T. Osborn, and P. Nasmyth, 1984: Local isotropy and the decay of turbulence in a stratified fluid. *J. Fluid Mech.*, **144,** 231–280.

Gibson, C. H., and W. H. Schwarz, 1963: The universal equilibrium spectra of turbulent velocity and scalar fields. *J. Fluid Mech.*, **16,** 365–384.

Gregg, M. C., 1984: Entropy generation in the ocean by small-scale mixing. *J. Phys. Oceanogr.*, **14,** 688–711.

——, 1987: Diapycnal mixing in the thermocline: A review. *J. Geophys. Res.*, **92** (C5), 5249–5286.

——, and T. B. Meagher, 1980: The dynamic response of glass-rod thermistors. *J. Geophys. Res.*, **85,** 2779–2786.

——, E. D'Asaro, T. Shay, and N. Larson, 1986: Observations of persistent mixing and near-inertial internal waves. *J. Phys. Oceanogr.*, **16,** 856–885.

Head, M. J., 1983: The use of miniature four-electrode conductivity probes for high resolution measurement of turbulent density or temperature variations in salt-stratified water flows. Ph.D. thesis, University of California at San Diego, 211 pp.

Holloway, G., A. Gargett, and B. Merryfield, 2001: Differential mixing in bistable conditions. *Proc. 'Aha Huliko'a Hawaiian Winter Workshop*, Manoa, HI, University of Hawaii, 187–190.

Itsweire, E., J. Koseff, D. Briggs, and J. Ferziger, 1993: Turbulence in stratified shear flows: Implications for interpreting shear-induced mixing in the ocean. *J. Phys. Oceanogr.*, **23,** 1508–1522.

King, D. B., and E. S. Saltzman, 1995: Measurement of the diffusion

coefficient of sulfur hexafluoride in water. *J. Geophys. Res.,* **100** (C4), 7083–7088.

Kolmogorov, A. N., 1941: The local structure of turbulence in an incompressible viscous fluid for very large reynolds numbers. *Dokl. Akad. Nauk.,* **30,** 299–303.

Kraichnan, R., 1968: Small-scale structure of a scalar field convected by turbulence. *Phys. Fluids,* **11,** 945–953.

Ledwell, J. R., A. J. Watson, and C. S. Law, 1993: Evidence for slow mixing across the pycnocline from an open-ocean tracer-release experiment. *Nature,* **364,** 701–703.

Luketina, D. A., and J. Imberger, 2001: Determining turbulent kinetic energy dissipation from batchelor curve fitting. *J. Atmos. Oceanic Technol.,* **18,** 100–113.

Merryfield, W. J., G. Holloway, and A. E. Gargett, 1998: Differential vertical transport of heat and salt by weak stratified turbulence. *Geophys. Res. Lett.,* **25,** 2773–2776.

Moum, J. N., 1990: Profiler measurements of vertical velocity microstructure in the ocean. *J. Atmos. Oceanic Technol.,* **7,** 323–333.

——, 1996a: Efficiency of mixing in the main thermocline. *J. Geophys. Res.,* **101** (C5), 12 057–12 069.

——, 1996b: Energy-containing scales of turbulence in the ocean thermocline. *J. Geophys. Res.,* **101** (C6), 14 095–14 109.

——, and J. D. Nash, 2000: Topographically induced drag and mixing at a small bank on the continental shelf. *J. Phys. Oceanogr.,* **30,** 2049–2054.

——, M. C. Gregg, R. C. Lien, and M. E. Carr, 1995: Comparison of turbulence kinetic energy dissipation rate estimates from two ocean microstructure profilers. *J. Atmos. Oceanic Technol.,* **12,** 346–366.

Nash, J. D., and J. N. Moum, 1999: Estimating salinity variance dissipation rate from conductivity microstructure measurements. *J. Atmos. Oceanic Technol.,* **16,** 263–274.

——, and ——, 2001: Internal hydraulic flows on the continental shelf: High drag states over a small bank. *J. Geophys. Res.,* **106** (C3), 4593–4611.

——, D. R. Caldwell, M. J. Zelman, and J. N. Moum, 1999: A thermocouple probe for high speed temperature measurement in the ocean. *J. Atmos. Oceanic Technol.,* **16,** 1474–1482.

Oakey, N. S., 1982: Determination of the rate of dissipation of turbulent energy from simultaneous temperature and velocity shear microstructure measurements. *J. Phys. Oceanogr.,* **12,** 256–271.

Osborn, T. R., and C. S. Cox, 1972: Oceanic fine structure. *Geophys. Fluid Dyn.,* **3,** 321–345.

Schmitt, R. W., 1979: Flux measurements on salt fingers at an interface. *J. Mar. Res.,* **37,** 419–436.

Smyth, W. D., 1999: Dissipation-range geometry and scalar spectra in sheared stratified turbulence. *J. Fluid Mech.,* **401,** 209–242.

——, and J. N. Moum, 2000: Anisotropy of turbulence in stably stratified mixing layers. *Phys. Fluids,* **12** (6), 1343–1362.

Sreenivasan, K. R., 1996: The passive scalar spectrum and the Obukhov–Corrsin constant. *Phys. Fluids,* **8** (1), 189–196.

Thompson, S., and J. Turner, 1975: Mixing across an interface due to grid turbulence generated by an oscillating grid. *J. Fluid Mech.,* **67** (2), 349–368.

Turner, J., 1968: The influence of molecular diffusivity on turbulent entrainment across a density interface. *J. Fluid Mech.,* **33,** 639–656.

——, 1973: *Buoyancy Effects in Fluids.* Cambridge University Press, 368 pp.

Washburn, L., T. F. Duda, and D. C. Jacobs, 1996: Interpreting conductivity microstructure: Estimating the temperature variance dissipation rate. *J. Atmos. Oceanic Technol.,* **13,** 1166–1188.